

PROJECTE FINAL DEL GRAU EN
ENGINYERIA FÍSICA

Dielectric Metal Dielectric Antireflection Plasmonic Layers

Eloi Ros Costals

Director: Joaquim Puigdollers Gonzalez (UPC)

UNIVERSITAT POLITÈCNICA DE CATALUNYA

Barcelona,
Juny 2017

Contents

0.1	Abstract	3
0.2	Acknowledgments	3
1	Introduction	4
1.1	Transparent conductive layers state of the art	4
1.2	Thesis outline	6
2	Theoretical background	7
2.1	Basics of solar cells	7
2.2	Introduction to thin film growth	12
2.3	Dielectric Metal Dielectric (DMD) structures	14
2.4	Simulation of optical properties of DMD	17
3	Fabrication and characterization of DMD structures	31
3.1	Equipment and facilities	31
3.2	Fabrication process	33
3.3	Fabrication and characterization of $MoO_3/Ag/MoO_3$ structures . .	34
3.3.1	$MoO_3/Ag/MoO_3/Glass$ structures	34
3.3.2	$MoO_3/Ag/MoO_3/c-Si$ structures	40
4	Fabrication and characterization of top electrode DMD c-Si solar cells	43
4.1	Design and fabrication of DMD based solar cell	43
4.2	Characterization of DMD based solar cell	46
5	Conclusion and future work	49

0.1 Abstract

In this work main research has been done as an attempt to optimize fabrication process of thin layers based DMD structures. Besides this technological aspect, a great characterization effort to optimize the DMD electrical and optical properties has been done.

Main fabrication and structural problems of this kind of structure are prime targets of this research as well as major benefits and possibilities of this technology from a broad perspective.

Finally due to future applications and market demands broadly studied silicon solar cells with TMO+ITO top carrier selective contact have been tried to be replaced by compact DMD structure top antireflection coating. Which possess carrier selectivity and increased conductivity that will allow fabrication of cheaper, flexible and functional indium-free solar cells.

0.2 Acknowledgments

I would like to thank Joaquim Puigdollers, for his support both moral and academic in my first step inside the world of research.

I would also like to thank Luis G. Gerling for the instruction in the clean room and advice during the research, as well as Cristóbal Voz for the fruitful discussions and assistance during several procedures inside and outside the clean room.

I would like to thank Joan Bertomeu from the UB, for assistance in photo-spectroscopy measurements. As well as Moises Garín, for the help regarding optimization of the simulations. I would also like to thank the rest of the group of UPC Electronic engineering department for their help in making fun and entertaining the research done in this project.

I would like to give a special thank to my friend Raül Perea, with whom I have shared many working hours in discussing about the physics involved in our respective projects, discussing results we were obtaining during the research and doing clean room procedures.

I would like to thank my friends for their support and interest during my project.

Finally I would like to thank all my family, my mother, my father and my sisters, as well as my aunts, uncles, cousins and grandparents. Thank you for your lifelong support.

Chapter 1

Introduction

1.1 Transparent conductive layers state of the art

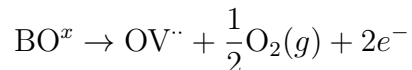
Recent interest towards flexible transparent electronics, as well as yield improvement of organic and silicon based energy harvesting devices, have made Transparent Conductive Oxides (TCO) a reliable option for many optoelectronic applications. Literature generally defines TCOs as doped metallic oxides typically with a greater transmittance than 80% and with a minimum carrier concentration of 10^{20} cm^{-3} [7].

Amongst this group one can find different types of TCOs, such as Fluorine doped tin Oxide (FTO) Aluminium doped Zinc Oxide (AZO) Gallium doped Zinc Oxide (GZO) and Indium Tin Oxide (ITO) . Even though there is a great variety of compounds within this family, ITO has had a dominant position due to its extraordinary optical and electrical properties. For instance, a 160 *nm* thick ITO layer has proved to achieve an averaged transmittance up to 95%[1]. Moreover a 20 order of magnitude lower resistivity than insulators ($\sim 10^{-4} \Omega \cdot \text{cm}$), which is still 4 orders of magnitude bigger than characteristic metal resistivity.

Most of TCO's available behave as n-type semiconductors with broad energy band gaps (i.e $\sim 3.2 - 3.5\text{eV}$). Large energy band gaps result in low photon absorption and increased optical transmittivity in low UV and Vis range of the spectrum. On the other hand conduction through TCO's arise from interstitial metal ion impurities, oxygen vacancies, and doping ions.

Metallic ion impurities and oxygen vacancies act as electron donors, first reason why this TCO's are mainly n-type. Oxygen vacancies are achieved using a reducing environment during TCO deposition. Taking ITO as an example, as Bonded Oxygen (BO) leaves it's original place in the lattice the vacancy left acts as a

doubly charged electron donor. The Oxygen Vacancy (OV) leaves In^{3+} ion 5s orbitals to be stabilized from the 5s conduction band by the missing bonds to the oxygen ion, at the same time two electrons are trapped at the site due to charge neutrality effects. Stabilization of the 5s orbitals causes a formation of a donor level for the oxygen ion determined to be 0.03 eV below the conduction band[6]. Electrons on this energy level have the potential to overcome the slight gap due to thermal excitation and step into the conduction band.



General applications of this thin conducting films can be found as conductive coatings in liquid crystal displays, flat panel displays, plasma displays and touch panels. But it is also widely extended in the field of OLEDs, and photovoltaics. In solar cells TCOs and ITO in particular, is a suitable material for front contact anti reflection coating. High light transparency and conductivity allows generated electrons/holes to be easily collected by the cell top metallic contact.

However, the limited supply of indium and the growing demand for ITO make the resulting fabrication costs prohibitive for future industry. Furthermore conductive ITO layers require a thickness of over 100 nm, thick enough ITO layers are known to be fairly brittle. Thus excluding ITO as a possibility in future flexible devices.

A number of strategies can be used as a replacement for ITO layer this is for instance metallic nano-wire composites (e.g. *Ag-nw/SnO_x*, *Cu-mesh/AZO*, *Ag-nw/MoO_x*), transparent conductive polymers most of which are derivatives of polyacetylene, polyaniline, polypyrrole or polythiophenes [2], as well as transparent conductive multilayer system based on ultra-thin metallic films[3].

Conductive polymers have highly tunable properties achieved by means of different structural composites, fabrication processes and adhesion of conductive polymers to strong textile and other kind of substrates[8]. Despite promising advances in the field, the scope of commercial uses remains rather small. Limitations of processability among polymers produced from commercially available monomers, poor environmental stability, low mechanical strength, and high cost have prevented conducting polymers from making a significant commercial impact[9].

Nano-wire composites on the other hand have a compromise between high conductivity (low R_{sheet}) and high transmittance. Represented as a factor of merit, ratio between direct current conductivity and optical conductivity gives large information on the compromise between optical and electrical properties of most of this nanowire composites. Some of which (e.g Ag and Cu NW-mesh in conductive polymer and insulators) are environmentally unstable[10].

Finally sandwiched structures based on ultrathin metallic layers have showed to achieve promising optical and electrical properties, on some applications it may already be a valid option over ITO due to cheaper nature of its compounds. In this new field of investigation most prominent investigated structures consist on dielectric metal dielectric, and metal dielectric metal multilayers.

1.2 Thesis outline

Transition Metal Oxides (TMOs) have proved to be an effective hole filter in crystalline silicon solar cells. Reported efficiencies reached for this type of cells get as high as 20% [42].

Most of the times, ITO is deposited on top of the TMO for improved carrier collection. Furthermore ITO also works as an antireflection layer for increased optical transmittance. Unfortunately ITO fabrication process requires scarce rare elements (i.e In), limiting its compatibility with large area, low cost devices.

Dielectric-Metal-Dielectric structures has emerged as one candidate to substitute ITO coatings on many applications. Actually some of the best DMD structures, in terms of their opto-electrical properties, were fabricated using TMOs as dielectric layers.

This opens the possibility to use TMO-based DMD structures in crystalline silicon solar cells, fulfilling two objectives. On one side, the use of TMOs layer in contact with the crystalline silicon will act as a hole filter, and, on the other hand, the overall DMD structure will be a replacement of the ITO layer.

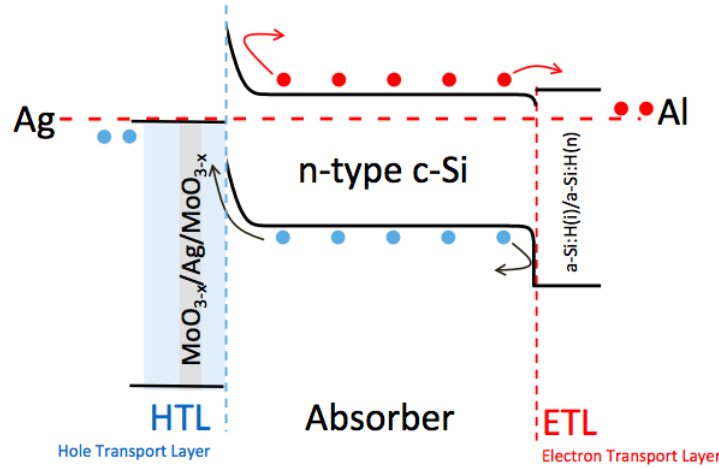


Figure 1.1: Band schematics of n-type crystalline silicon solar cell with top DMD selective contact

Chapter 2

Theoretical background

2.1 Basics of solar cells

Principles of operation

A solar cell is by definition an electrical device that converts the energy of light directly into electricity by means of the photoelectric effect. Semiconductors possess a spectrum of strongly attached and free electronic states energetically separated by a gap called bands. Low energy gap allows greater electric properties than insulators, and the existence of this gap of forbidden states increases the time required in relaxation processes, this yields greater probability to collect generated current. Bonded electrons (i.e. electrons on the valence band E_V) are strongly attached and thus not able to flow through the solid, while energetic electrons (i.e. electrons on the conduction band E_C) are perfectly able to conduct electricity. Charge carriers are generated in the semiconductor through electronic transition

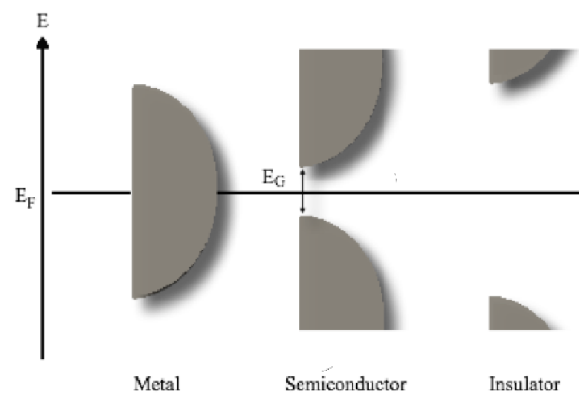


Figure 2.1: Band representation on different type of materials

from a state on the valence band to a state on the conduction band. When a photon with an energy higher than the gap ($\hbar\omega > E_G$) is absorbed by a valence band electron, this acquires enough energy to occupy a state in the conduction band, becoming able to easily flow through the material. Consequently, an electron vacancy is generated in the valence band, this vacancy also behaves as a charge carrier. Due to its generation nature this carrier is called a *hole*. Holes conduction is understood if one considers that an electron vacancy on the valence band can be occupied by a neighbor valence electron due to an external perturbation such as the effect of an electric field. Displacement of the vacancy generates a charge movement that in overall could be accounted as a single carrier with positive charge and different electrical behaviour than electrons.

If the electron generated has absorbed a high energy photon a very energetic state can be occupied by this carrier, obviously the continuous spectrum of states allow the carrier to gradually lose the energy by generating phonons until it reaches the minimum energy level E_C value. Once the carrier has reached the minimum energy point of the conduction band, it may only stabilize back to the valence band by losing exactly E_G or more energy.

Recombination

Needless to say, the greater problem with generated carriers are the tendency of the excited electrons to return to its original equilibrium state. By this means electrons spontaneously find holes that stabilize them back into a valence band states, this process is called recombination. Recombination speed is defined as a function of the carriers lifetime (τ)[11].

Different types of recombination processes are caused by different physical effects. Radiative recombination is the opposite effect of carrier generation, electron/hole pair recombines and the material emits a photon. It is most common in direct gap semiconductors while very uncommon in indirect gap type semiconductors like silicon. Auger recombination is the stabilization of the carrier due to energy transference to a third carrier. Shockley-Read-Hall (SRH) recombination [12,13] is due to imperfections and crystallographic defects. As they act as electron/hole recombination centers. In low carrier injection major concern in carriers lifetime is due to SRH recombination, while in high injection conditions carriers lifetime is limited by Auger and Radiative type of recombination.

Finally in crystalline silicon, a specific type of recombination is generated due to rough end of the crystallographic net. Free silicon bonds and impurities are the main source of this superficial type of recombination.

Regarding all types of recombination one can estimate the total recombination

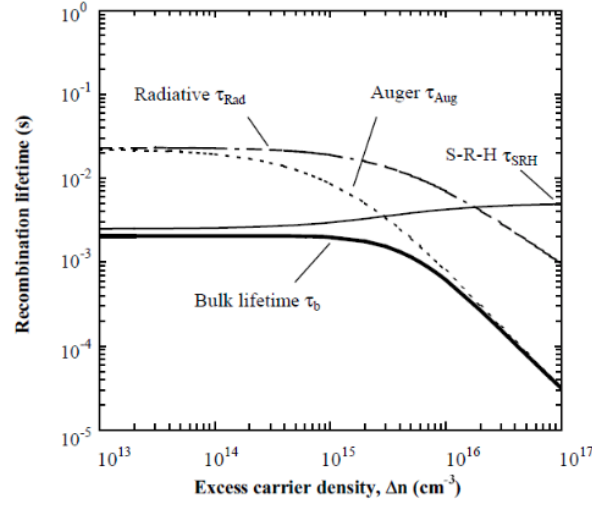


Figure 2.2: Recombination lifetime as a function of carrier injection

speed using lifetime below

$$\frac{1}{\tau_{eff}} = \left(\frac{1}{\tau_{SRH}} + \frac{1}{\tau_{Auger}} + \frac{1}{\tau_{rad}} \right) + 2 \cdot \frac{S_{eff}}{W}$$

Usually bulk recombination is not comparable to superficial recombination. By this means one can drastically improve cell behaviour by increasing superficial passivation.

Basics of semiconductor physics

A basics on semiconductors physics must be introduced in order to understand physical phenomena involved in a solar cell, by this means one must introduce first the *Density Of States* (DOS) of the semiconductor.

As electrons move in a particular direction on a semiconductor crystal, their movement can be described as standing-wave oscillations with a characteristic wavelength λ , multiple of the semiconductor length L .

In a generic 3D crystalline case with $n_{[i,j,k]} \cdot \lambda = L$, where $n_{[i,j,k]}$ corresponds to natural numbers in each axis direction, and $p_{[x,y,z]} \lambda = h$ from De Broglie relation, one gets the relation between the volume for an energy state in the momentum space. Using the kinetic energy relation for an electron $E_{e^-} = \frac{p^2}{2m_e}$ one finally gets an expression on the DOS.

$$DOS(E > E_C) = \frac{8\pi\sqrt{2}}{h^3} m_e^{* \frac{3}{2}} \sqrt{E - E_C}$$

$$DOS(E < E_V) = \frac{8\pi\sqrt{2}}{h^3} m_h^* \sqrt{E_V - E}$$

The DOS tells us the number of energy eigenstates per unit energy range, and it can be seen how this depends on the $E(\vec{k})$ relationship. [14]

With knowledge of the distributed available states as well as the occupation probability of this states described in Fermi-Dirac statistics one can calculate the number of bulk charge carriers.

$$F(E) = \frac{1}{1 + e^{\frac{E-E_F}{k_B T}}} \cong e^{-\frac{E-E_F}{k_B T}}$$

$$n = \int_{E_c}^{\infty} DOS(E) \cdot F(E) dE \approx N_C e^{\frac{E_F - E_C}{k_B T}}$$

$$p = \int_{-\infty}^{E_V} DOS(E) \cdot F(E) dE \approx N_V e^{\frac{E_V - E_F}{k_B T}}$$

Where $N_C = 2 \left(\frac{2\pi m_e^* k_B T}{h^2} \right)^{\frac{3}{2}}$ and $N_V = 2 \left(\frac{2\pi m_h^* k_B T}{h^2} \right)^{\frac{3}{2}}$ describes the effective density of states in conduction and valence bands.

Semiconductors generally poses intrinsic behaviour, this means that it has the same amount of positive and negative bulk carriers.

From characteristic intrinsic carrier concentration one gets the Law of Mass action.

$$n \cdot p = n_i^2 = N_C N_V e^{\frac{-E_G}{k_B T}}$$

Through doping processes one can achieve larger concentration of a certain type of carriers (i.e. n for negative type carrier concentration and p for positive type). This type of semiconductors are called extrinsic.

In low injection conditions applying charge carrier neutrality on the semiconductor ($n + N_A = p + N_D$) and Law of mass action one can still find carriers concentration on extrinsic semiconductors. Being N_A acceptor impurities and N_D donor impurities concentration.

Electrical current on semiconductors is generally due to diffusion and electrical drift effects. Carriers diffuse in the direction of the concentration gradient following Fick's law as well as by means of an electric field following Ohm's law. Using this, current can be established as $J_T = J_p + J_n$ where:

$$J_n = q\mu_n n \vec{E} + qD_n \frac{dn}{dx}$$

$$J_p = q\mu_p p \vec{E} - qD_p \frac{dp}{dx}$$

Quasi-Fermi level

Due to light irradiation that takes place during working conditions of solar cells large generation of electron/hole pairs unbalance the law of mass action. Consequences of the large amount of electrons generated should be an approach of the Fermi level of the electrons distribution to E_C as well as an approach to E_V by holes Fermi distribution. Using this outside of equilibrium Fermi levels (i.e quasi-Fermi levels) one can validate a new law of mass action by means of:

$$np = n_i^2 e^{-\frac{E_{FV} - E_{FC}}{k_B T}}$$

Electron/Hole collection

Understanding of charge carrier separation is broadly treated in [17,15], a short explanation on this effect can be explained based on S.Datta [14,16].

Given a source of electrons, a drain, and a channel that connects them, source (μ_1) and drain (μ_2) will possess same electrochemical potential (μ_i) unless a bias tension is applied ($\mu_1 = \mu_2 + qV$), and no current will flow otherwise. Gradient of electrochemical potential motivates electrons to flow occupying free states available on the channel therefore reaching minimum free energy once collected on the drain.

Using this approach, the movement of the carriers inside the cell can be understood as a consequence of a gradient of their quasi-Fermi level .

Finally electrons are blocked on one of the contacts and holes on the other, this way all carriers collected generate a current on the same direction. Materials used for this purpose may act as Electron Transport Layer (ETL) which allows high electron selectivity and prevent holes to be collected, or as Hole Transport Layers (HTL) which allows holes to be collected (injects electrons from the contact) and prevents electrons on the wafer to be collected.

As clearly stated in this work, properly tuned workfunctions of TMO can be used as HTL in silicon solar cells. As carriers are generated inside the absorber, holes and electrons move due to diffusion generated by its curved quasi-Fermi level.

As can be seen in fig(1.1), multilayer system under study can work perfectly as a HTL. Furthermore at the same time because of its high sheet conductivity due to silver metallic mid layer, it allows easy movement of the generated charge carriers towards the metallic top contacts.

2.2 Introduction to thin film growth

As micro and opto electronics industry is advancing towards miniaturization of their devices, new techniques have to be developed to fabricate nanometer dimension structures.

A thermal evaporator works with basic thermodynamic principles, taking an isobar process, increase of the temperature affects the internal energy of the material related directly to the kinetic energy of its particles by statistical mechanics.

Under a high vacuum chamber a crucible holding the material in a solid state transfers by thermal conduction the energy directly to the desired material. Heat generation is directly done by joule effect on the crucible induced by electrical current.

Low environmental pressure provided by vacuum pump inside the chamber decreases sublimation, or melting and boiling point as may be seen for iron in figure below.

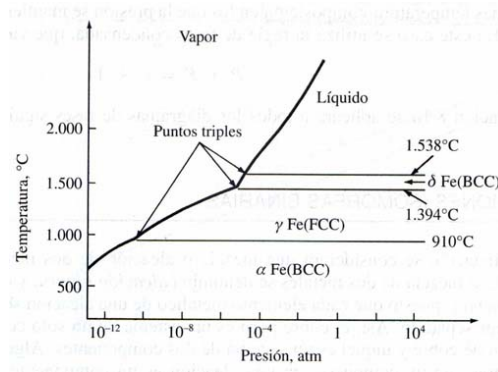


Figure 2.3: Illustrative phase diagram of iron

In addition, high vacuum increases dramatically mean free path of evaporated particles as they don't find obstacles in the middle of their path to the target. Finally, low temperature substrate condensates the material on top of the target and a layer starts to grow. [18]

When evaporated most of solid materials doesn't generate a perfectly uniformly distributed layer ($d(\theta) \propto \cos(\theta)$), several techniques like target location and rotation decrease effects of this kind.

Presence of oxidizing or reducing agents may alter the chemical composition of many evaporated materials, reducing the amount of vapor generated and making deposition difficult to control as well as affecting the growing layer.

Literature on the matter explains three possible modes of thin film growth on surfaces[43].

Frank-Van der Merwe or layer by layer growth, implies that when the atom deposited falls onto the substrate, it tends to bond to the substrate atoms because of the greater wetting effect between deposited and substrate atoms. By this means at the initial nucleation stage the film will take a large two-dimension character. As a result, it will form a complete monolayer by uniformly distributing deposited atoms on the surface of the substrate. As a consequence atoms deposited on top will grow as a uniform film.

Volmer-Weber or island growth mode occurs when deposited atoms have large cohesion forces, this means that these materials have a greater tendency to bind to each other than to bond to the substrate atoms. This effect is mainly due to the poor wetting effect between the deposited atom and the substrate atoms. As a consequence the film grows into a rough surface with significant topographic features. This type of growth is generally displayed by many soft metals such as gold, silver and copper grown on insulators[19].

Stranski-Krastanov growth also called island plus layer growth is an intermediate case. During initial nucleation and growth stage it behaves as a *Frank-Van der Merwe* material, but during the subsequent growth it starts behaving as a *Volmer-Weber* material.

Nanometric dimension and well behaved optoelectronic devices may be achieved by deposition of atomically smooth films. Fabrication methods that enhance a layer by layer growth modes are preferable.

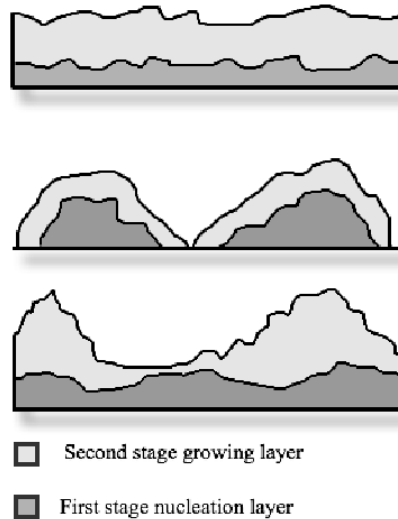


Figure 2.4: Representation of Frank-Van der Merwe, Volmer-Weber and Stranski-Krastanov type of layer growing

2.3 Dielectric Metal Dielectric (DMD) structures

Most of available solutions in the quest for indium free transparent conductive layers require specific lab conditions and procedures, not reproducible in industrial fabrication process. Thermally evaporated or sputtered multilayer systems based on ultra-thin metallic films such as DMD structures could become an inexpensive efficient option to replace ITO in a short-mid term.

DMD structures was first proposed for increasing ITO conductivity [20] as ITO is a great TCO in the case of small surface, but for large area devices it induces series resistance that decreases the device efficiency.

A multilayer of ITO/Metal/ITO was found to have increased flexibility since ITO thick layers are known to be brittle. Towards fabrication of *In* free electrodes ITO layers were replaced by metallic layers sandwiched with TCOs. And due to energetic nature of particle deposition in sputtering process, which may damage the substrate in case of organic devices, DMD research took a change of direction into soft deposition techniques such as thermal evaporation [21].

On overall one can use as top and bottom dielectric layers TCOs such as ITO, conductive polymers such as PEDOT and metallic oxides such as MoO_3 , WO_3 or V_2O_5 . By this means one can use several types of materials as top and bottom dielectric layers, fitting a better work-function, refractive index, conductivity and other intrinsic characteristics depending on the application required.

Recent critical review has been dedicated to TCO/Metal/TCO multilayers[22]. It is shown that *silver* and *ITO* gives the best results on conductivity ($\rho_{ITO/Ag/ITO} = 1.6 \mu\Omega \text{ cm}$, $\rho_{ITO/Au/ITO} = 1.7 \mu\Omega \text{ cm}$, $\rho_{ITO/Cu/ITO} = 2.4 \mu\Omega \text{ cm}$).

Since the equivalent circuit can be understood as 3 parallel resistances, it is only logical to think that the resistance of the structure will be mainly related to that of the metal film.

$$R_T^{-1} = \frac{1}{R_{Metal}} + \frac{1}{2R_{Oxide}}$$

As may be seen in many literature results on DMD research (e.g [33]), a threshold on the conductivity due to metallic mid layer thickness becomes crucial also on optical properties. The threshold thickness value corresponds to the percolation of the metal nanostructures.

As stated in the previous section, soft metals like silver gold or copper, have a *Volmer-Weber* likewise type of growing. This means that they tent to form rough layers from an island like growing. As good optical properties are mainly due to absorption and reflection on the silver layer, one will have to use ultrathin metallic layers and minimum possible amount of metal.

If one goes to low values of deposited material, islands formed on the substrate won't be able to connect among themselves (i.e percolation of the metal nanostructures). Discontinuity of the metallic path on a nanometric scale increase

dramatically the resistance of the multilayer structure to near insulator values ($\propto 10^6\Omega$). For a thick enough metallic deposition a pseudo-homogeneous layer is achieved, and typical metallic conductivity regained enhances the device conductivity to orders of magnitude.

Interesting enough is the fact that for extremely thin highly percolated layers, great optical properties are achieved (i.e low opacity). While if one increases metallic thickness opacity increases dramatically.

With this said, once homogeneous layer is finally achieved at conductivity threshold, and the DMD is electrically conductive, optical transmittance increases with the metal thickness up to a critical value. Finally as it would be expected, opacity grows proportional to the metallic layer thickness.

Initial opacification can be understood if one consider that when larger and larger islands of metals are deposited active surface of the metal increases and thus reflection and absorption of the device.

Moreover, at this stage surface plasmons (SP) vector wave couples with incoming light vector wave, thus increasing absorbed light of the device due to generation of this SP. Once the layer becomes homogeneous frequency dependant effective dielectric and metallic permittivity (i.e ϵ_d ϵ_m) shifts to values that decreases plasmonic coupling effects[40]. As resonance between incoming light and surface plasmons is avoided, classical multiple reflections on the multilayer interfaces account for grater transmittance.

Increased transmittivity with thickness of the metallic layer on the multilayer system is then explained as a consequence of a smothering process of the middle layer roughness. With flatter homogeneous layer and fine tuning of top and bottom thickness dielectric one can achieve an increased light transmission than just a ultrathin metallic layer.

Finally as one increases metallic thickness beyond the critical value opacity increases directly proportional to this layer as one would expect from classical electromagnetic theory.

First semitransparent electrode based on thermally evaporated DMD reported consisted on a structure of $WO_3(40\text{ nm})/Ag(12\text{ nm})/WO_3(40\text{ nm})$ with a sheet resistance of $R_{sh} = 6\Omega sq^{-1}$ and a transmittance of 90% at 550 nm [23].

Whereas MoO_3 and WO_3 have rather similar electronic and optical properties clear advantage of MAM ($MoO_3/Ag/MoO_3$) over WAW ($WO_3/Ag/WO_3$) is that MAM DMD's can be evaporated at substantially lower temperature when compared to WAW, which can be useful when used in devices sensitive to high temperatures.

There is a debate on whether aggregation of Ag layers on top of ZnS is suppressed (i.e island addition after deposition), as well as improved thermal stability of percolated Ag layers. By this means hybrid electrodes such as $ZnS/Ag/MoO_3$

$ZnS/Ag/WO_3$ have been studied [24,25].

Besides Ag as the main metal on DMD structures with MoO_3 , or WO_3 one can use Cu Au and Al . A potential problem for this kind of structures is the diffusion of the metal inside the dielectric layers. For the case of silver and copper this diffusion is most accentuated, and a very thin layer of aluminum or gold can be used to prevent this effect (e.g 1 nm). [26]

Use of different metallic layers as seed or wetting layer could be done as a previous step of the deposition of the metal mid-layer, if the material has an accentuated *Volmer-Weber* behaviour. For example in [27] gold, aluminum and calcium seed layers are tested. It is seen that for 1 nm gold seed layer a DMD with 3 nm silver thickness has already a $R_{sh} \approx 3k\Omega/sq$ which is orders of magnitude below typical sheet resistance without wetting layer ($R_{sh} \approx 10^6\Omega/sq$). With a 5 nm silver layer a $R_{sh} \approx 88\Omega/sq$ is achieved which already is comparable to ITO typical sheet resistance.

In [28] a pseudo-alloy of silver and aluminum (i.e silver doped with aluminum through co-sputtering process) is studied as aluminum presence can be a smothering factor of the surface roughness when depositing a silver ultrathin layer.

Finally, oxides most used as dielectric layers such as MoO_3 V_2O_5 and WO_3 , are known to have large work functions and enhanced conductivity due to oxygen vacancies generated during the deposition. An interesting result that indicates us that this materials can be used as hole transport layer in c-Si based solar cells.

Already studied by the UPC *Electronic engineering department* in [4] transition metal oxides such as V_2O_5 MoO_3 WO_3 and ReO_3 , were thermally evaporated as front p-type contact in planar n-type crystalline silicon heterojunction. And solar cells with intrinsic thin layer (HIT) have been successfully fabricated with Power Conversion Efficiency (PCE) up to 12.7%. For the case of top anti reflection coating of " $MoO_3 + ITO$ " electrical properties revealed $J_{sc} = 29.6mA/cm^2$, $V_{oc} = 581mV$, $FF = 73.1\%$ $PCE = 12.6\%$. Stated in [29] using a MAM DMD as top anti-reflection coating on a c-Si heterojunction with HIT structure. Results obtained yielded electric characteristics of $J_{sc} = 29.43mA/cm^2$, $V_{oc} = 583mV$, $FF = 75.83\%$ $PCE = 13.01\%$. Which implies that ITO could be successfully removed from typical front contacted solar cells without any major downside.

Further study from UPC *Electronic engineering department* group revealed PCE for this TMO+ITO top structure reached a value of 15.7% for V_2O_5 [41]. Which indicates that further improvement has to be done to this type of indium free c-Si solar cells, either by optimization of the structure, or DMD implementation in Interdigitated back contact (IBC) type of solar cells as bottom selective contacts.

2.4 Simulation of optical properties of DMD

Mathematical approach

First approach to DMD fabrication consists on theoretical optimization of the multiple layers in order to increase as much as possible optical transmittance. Even though as commented in the previous section, deposition of the metallic layers involves large technological problems (i.e deposition of topologically rough and non uniform layers), in this simulation perfectly flat homogeneous and isotropic metallic layers will be assumed.

A slightly shorter explanation and demonstration than in literature [30,31] will be done to introduce the method used for the simulations.

The first typical mathematical approach will consist on a monolayer coating.

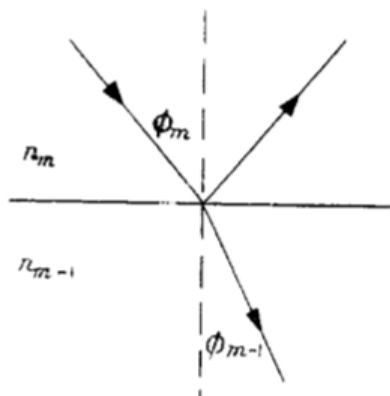


Figure 2.5: Representation of the m^{th} layer field interaction

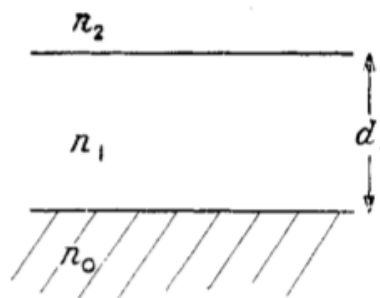


Figure 2.6: Monolayer coating

Quick analysis on a parallel polarization monochromatic wave will give us the transmission and reflection coefficients. Considering incident, reflected, and transmitted fields to have the expression:

$$\begin{aligned}\vec{E}_i &= E_{0i}(\hat{y}\cos(\phi_i) - \hat{z}\sin(\phi_i))e^{-j\vec{k}_i \cdot \vec{r}}, \vec{H}_i = -\hat{x}\frac{E_{0i}}{\eta_1}e^{-j\vec{k}_i \cdot \vec{r}} \\ \vec{E}_r &= E_{0r}(\hat{y}\cos(\phi_r) + \hat{z}\sin(\phi_r))e^{-j\vec{k}_r \cdot \vec{r}}, \vec{H}_r = \hat{x}\frac{E_{0r}}{\eta_1}e^{-j\vec{k}_r \cdot \vec{r}} \\ \vec{E}_t &= E_{0t}(\hat{y}\cos(\phi_t) - \hat{z}\sin(\phi_t))e^{-j\vec{k}_t \cdot \vec{r}}, \vec{H}_t = -\hat{x}\frac{E_{0t}}{\eta_2}e^{-j\vec{k}_t \cdot \vec{r}}\end{aligned}$$

After applying boundary conditions of the type:

$$\hat{n}(\vec{E}_2 - \vec{E}_1)\Big|_S = \vec{0}$$

$$\hat{n}(\vec{H}_2 - \vec{H}_1)\Big|_S = \vec{J}_s$$

One finds an expression for the transmission and reflection coefficient defined as:

$$r_{//} = \frac{E_r}{E_i} = \frac{n_1 \cos(\phi_t) - n_2 \cos(\phi_i)}{n_1 \cos(\phi_t) + n_2 \cos(\phi_i)}, t_{//} = \frac{E_t}{E_i} = \frac{2n_1 \cos(\phi_i)}{n_1 \cos(\phi_t) + n_2 \cos(\phi_i)}$$

The same procedure for perpendicular polarization yields:

$$r_{\perp} = \frac{E_r}{E_i} = \frac{n_1 \cos(\phi_i) - n_2 \cos(\phi_t)}{n_1 \cos(\phi_i) + n_2 \cos(\phi_t)}, t_{\perp} = \frac{E_t}{E_i} = \frac{2n_1 \cos(\phi_i)}{n_1 \cos(\phi_i) + n_2 \cos(\phi_t)}$$

Snell's law gives us a relation between the income and outcome angles:

$$n_1 \sin(\phi_i) = n_2 \sin(\phi_t)$$

Knowledge of this coefficients gives us an expression of the transmitted and reflected field initial amplitude, damping and oscillation of the field will be proportional to the exponential of the refractive index complex and real part times the distance (i.e $E(z) \propto \exp(-i(n - ik) \cdot z)$). A notation change will be introduced now for later systematization to n layers. Income index will have the greater value (m) while substrate index will be always (0). So on a more general case this becomes:

$$r_{m//} = \frac{n_m \cos(\phi_{m-1}) - n_{m-1} \cos(\phi_m)}{n_m \cos(\phi_{m-1}) + n_{m-1} \cos(\phi_m)}, t_{m//} = \frac{2n_m \cos(\phi_m)}{n_m \cos(\phi_{m-1}) + n_{m-1} \cos(\phi_m)}$$

$$r_{m\perp} = \frac{n_m \cos(\phi_m) - n_{m-1} \cos(\phi_{m-1})}{n_m \cos(\phi_m) + n_{m-1} \cos(\phi_{m-1})}, t_{m\perp} = \frac{2n_m \cos(\phi_m)}{n_m \cos(\phi_m) + n_{m-1} \cos(\phi_{m-1})}$$

By this means transmission and reflection coefficients onto the substrate in the monolayer case becomes:

$$R = \frac{r_2 + r_1 e^{-2i\delta_1}}{1 + r_1 r_2 e^{-2i\delta_1}}$$

$$T = \frac{t_1 t_2 e^{-i\delta_1}}{1 + r_1 r_2 e^{-2i\delta_1}}$$

where $\delta_1 = 2\pi \frac{n_1}{\lambda} d_1 \cos(\phi_1)$

For non-normal incidence R and T each yield two equations corresponding to each plane of polarization. Energies crossing unit area per second normal to the reflected and transmitted beams are given by:

$$\mathbf{R} = RR^* = \frac{r_2^2 + 2r_1 r_2 \cos(2\delta_1) + r_1^2}{1 + 2r_1 r_2 \cos(2\delta_1) + r_1^2 r_2^2}$$

$$\mathbf{T} = \frac{n_2}{n_0} TT^* = \frac{n_2}{n_0} \frac{t_1^2 t_2^2}{1 + 2r_1 r_2 \cos(2\delta_1) + r_1^2 r_2^2}$$

As for normal incidence $r_{1,2}$ and $t_{1,2}$ becomes:

$$r_2 = \frac{n_2 - n_1}{n_2 + n_1}, t_2 = \frac{2n_2}{n_2 + n_1}$$

$$r_1 = \frac{n_1 - n_0}{n_1 + n_0}, t_1 = \frac{2n_1}{n_1 + n_0}$$

R and T calculated may still be used for the case of absorbing media. The values used of n in evaluating Fresnel coefficients and in the δ_1 term may be replaced by complex $\mathbf{n} = n - ik$. Values of the phase obtained now by Snell Law will be now complex, a manifestation of the fact that in an absorbing medium the planes of constant amplitude may be inclined to the planes of constant phase of the wave. Calculation of the reflectance and transmittance of a system of parallel-sided films may be done by systematic layer by layer analysis and a stepwise unknown variables computing (i.e effective reflection and phase change). For a system of k layers, amplitude reflection coefficient for the first film may be written as:

$$\rho_2 e^{i\Delta_2} = \frac{r_2 + r_1 e^{(-2i\delta_1)}}{1 + r_1 r_2 e^{(-2i\delta_1)}}$$

where r_2, r_1 are the Fresnel coefficients for n_2/n_1 and n_1/n_0 interfaces and ρ_i and Δ_i step by step calculated unknowns. Reflection of the coefficient for the first two films may then be written as:

$$\rho_3 e^{i\Delta_3} = \frac{r_3 + \rho_2 e^{i\Delta_2} e^{(-2i\delta_1)}}{1 + r_3 \rho_2 e^{i\Delta_2} e^{(-2i\delta_1)}}$$

The m^{th} layer this becomes:

$$\rho_m e^{i\Delta_m} = \frac{n_{m+1} - N_m}{n_{m+1} + N_m}$$

$$\frac{N_m - n_m}{N_m + n_m} = \frac{N_{m-1} - n_m}{N_{m-1} + n_m} e^{-4\pi i \frac{n_m}{\lambda} d_m}$$

As \mathbf{R}_k and \mathbf{T}_k results:

$$\mathbf{R}_k = \left| \frac{n_{k+1} - N_k}{n_k + 1 + N_k} \right|^2$$

$$\mathbf{T}_k = \frac{4n_0 n_{k+1}}{(n_1 + n_0)^2} \prod_1^k \left| \frac{N_m + n_m}{N_m + n_{m+1}} \right|^2$$

A disadvantage of this method of calculation is that if the effect of altering the thickness or refractive index of any layer in the system is being studied, then the procedure given above must be repeated for all layers subsequent to the one changed. This drawback can be avoided in the matrix method.

Equations relating the amplitude of successive media can be conveniently written in matrix notation. Which is the most convenient treatment for computation. This, if we denote E_m^+ the amplitude of the electric vector of the wave travelling in the direction of incidence in the m^{th} and E_m^- , solutions of the equations of propagation readily yields the following relations:

$$E_m^+ = t_m^{-1} [E_{m-1}^- e^{i\delta_{m-1}} + r_m E_{m-1}^- e^{-i\delta_{m-1}}]$$

$$E_m^- = t_m^{-1} [r_m E_{m-1}^+ e^{i\delta_{m-1}} + E_{m-1}^- e^{-i\delta_{m-1}}]$$

which can be written as:

$$\begin{pmatrix} E_m^+ \\ E_m^- \end{pmatrix} = \frac{1}{t_m} \begin{pmatrix} e^{i\delta_{m-1}} & r_m e^{-i\delta_{m-1}} \\ r_m e^{i\delta_{m-1}} & e^{-i\delta_{m-1}} \end{pmatrix} \begin{pmatrix} E_{m-1}^+ \\ E_{m-1}^- \end{pmatrix} = \frac{1}{t_m} M_{m-1} \begin{pmatrix} E_{m-1}^+ \\ E_{m-1}^- \end{pmatrix}$$

For a stack of k layers onto a substrate this becomes:

$$\begin{pmatrix} E_{k+1}^+ \\ E_{k+1}^- \end{pmatrix} = \frac{M_k M_{k-1} \dots M_2 M_1}{t_k t_{k-1} \dots t_2 t_1} \begin{pmatrix} E_0^+ \\ E_0^- \end{pmatrix}$$

Finally optical Transmittance and Reflectance can be calculated as:

$$\mathbf{R} = \frac{|E_{k+1}^-|^2}{|E_{k+1}^+|^2}$$

$$\mathbf{T}_{//} = \frac{n_0}{n_{k+1}} \frac{|E_0^+|^2}{|E_{k+1}^+|^2}$$

$$\mathbf{T}_{\perp} = \frac{n_0 \cos^2(\phi_{k+1})}{n_{k+1} \cos^2(\phi_0)} \frac{|E_0^+|^2}{|E_{k+1}^+|^2}$$

Results

A code was written on python to approach this multilayer coatings from the presented theoretical point of view. This way one can study how interference's on the system affects to overall optical properties. As a source code to calculate successive M_k needed it has been used a compact optimized version provided by *Dr. Moisés Garín*.

The values of n and k were extracted for MoO_3 , Ag , $c-Si$ and all other miscellaneous materials used in this series of simulations, from [32].

It's fair to say that assumptions on the geometry and optical behaviour of the multilayer structure are rather strong conditions that are not that near to what one has in reality, so a perfect fit of the results is not expected. Besides typical error from idealization, it has been seen that high extinction coefficient value (e.g metals) in materials used in this type of simulations can induce to mathematical error, thus making results from the simulation not 100% accurate, even for an ideal case. Small thickness of this metallic layers, and ensuring that input and output materials do not possess this high extinction coefficients will be enough to limit this type of error and obtain a qualitative guide towards fabrication of this structure.

Better approach to this problem can be achieved through finite difference time domain (FDTD) method. This method is able to rigorously solve the Maxwell's equations and makes it possible to obtain the electromagnetic field as a function of time and position. Use of FDTD as well as use of effective n and k values of percolated thin silver layers as it is done in [34] may be done as future work to achieve more accurate results. Using measured results in [33,34], a comparison with simulated results is going to give us an idea of the veracity of the simulation. Measured transmittance is done on glass, and for the simulations calculated transmittance corresponds to $c-Si$ substrate, this may yield a certain bias.

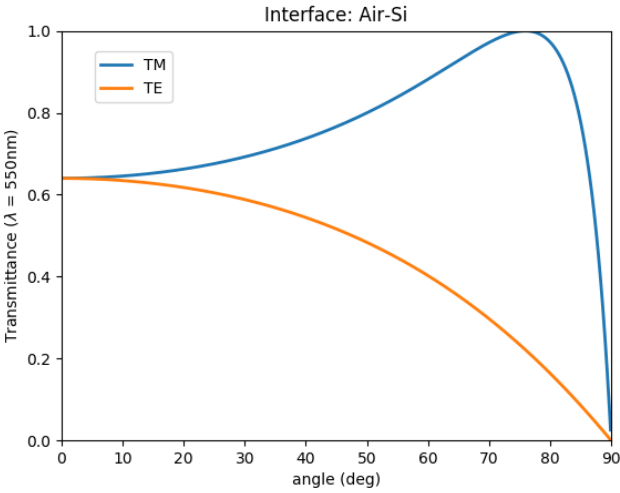


Figure 2.7

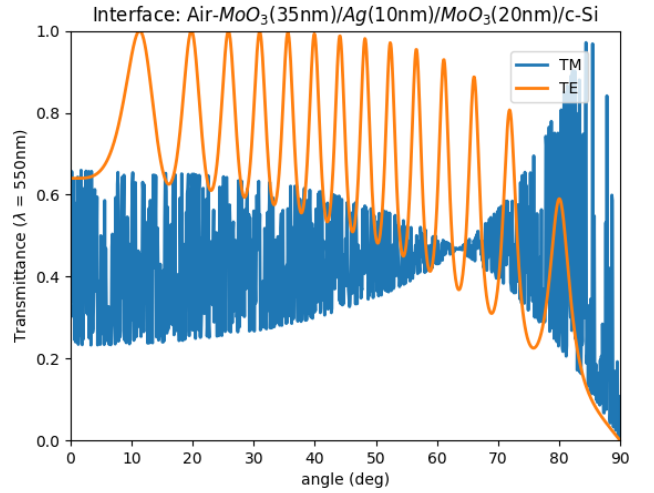


Figure 2.8

Nevertheless as a first approach to DMD numerical characterization, fixing $\lambda = 550nm$ and taking as an approximated values $n_{MoO_3} = 2$, $n_{c-Si} = 4$ and $n_{Ag} = 0.05 + 5i$. One can see how under different income angle a huge difference

is appreciated in the behavior of transmitted TE and TM modes when a 20/10/35 (nm) DMD is deposited on the top of a silicon semi-infinite wafer. For the TE mode one can rapidly see in fig(2.7) and fig(2.8) that the Air/c-Si curve is actually the lower bound of the DMD/c-Si case. Which implies that besides this visible oscillations the tendency without the coating remains.

Oscillations on the transmittance as a function of the income angle are not taken into account on further simulations since for simplicity only normal incidence will be considered. Even though this result could be thought as a positive result for proving that DMD's can properly work as anti-reflection coatings.

Unfortunately for TM a rapid and confusing oscillatory behaviour is obtained from the simulations. Therefore, no consistent conclusions can be obtained from it.

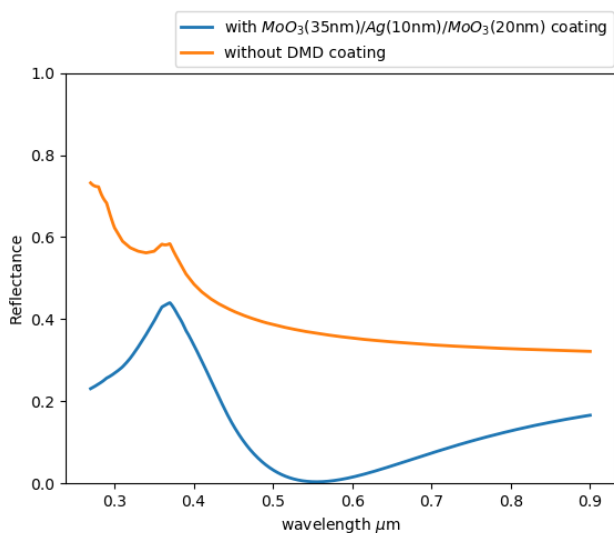


Figure 2.9

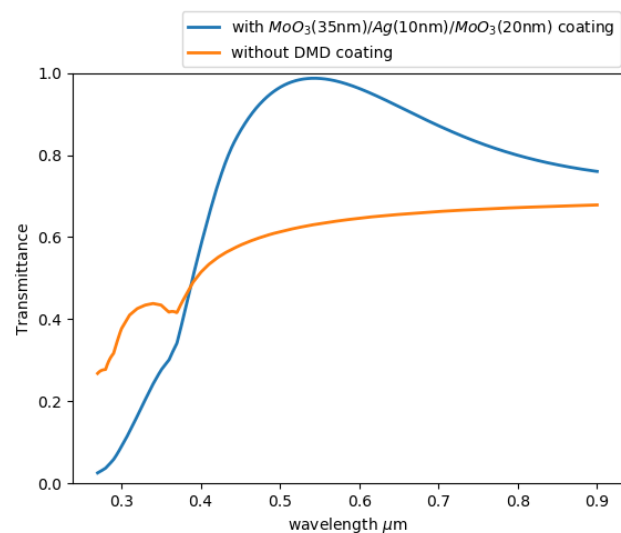


Figure 2.10

A more realistic set up, and potentially reproducible when measuring the actual fabricated DMDs, is a spectrum of the optical properties as a function of incoming light wavelength. In this case, reflectance transmittance and absorbance have been calculated for a typical 35nm/10nm/20nm DMD in a spectral window between 270nm and 900nm. Absorbance has been obtained from relation:

$$P_{Absorbed} = P_{Total} - P_{Transmitted} - P_{Reflected}$$

As it is shown in fig(2.10) and fig(2.9), a window of high transmittance and low reflectance is achieved in Vis-NIR part of the spectrum. Transmittance curve is consistent with real behaviour of DMD's reported by L.Cattin, J.C Bernède *et al* in [33]. As one can appreciate the same type of maximum is achieved in the

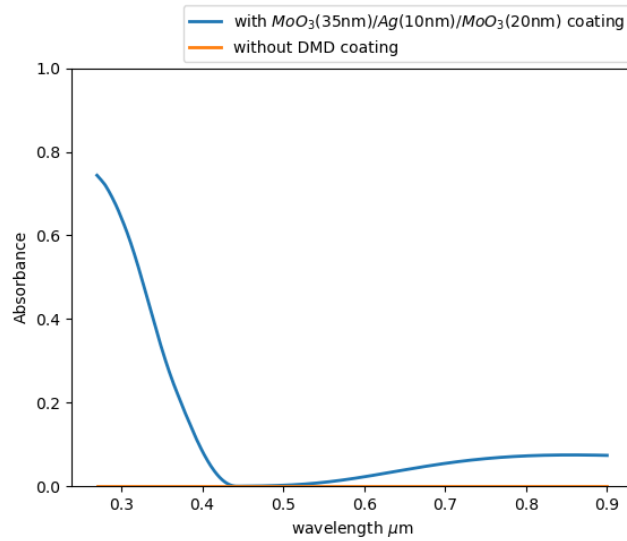


Figure 2.11

Visible part of the spectrum near the $500nm$ wavelength, and rapid decrease in UV-NIR part of the spectra gives consistence in the results obtained.

A very high absorption of the multilayer in the UV is observed but no measures can be used to contrast veracity of this result, as it can be thought that this peak might be a mathematical induced error due to high extinction coefficient of the silver layer as comented before. Besides the high absorption peak, shape similarities in transmittance curve with the real results may lead us to some other results regarding transmitted light.

As one can see, a study of the change in transmittance has been made as a function of top and bottom MoO_3 layer thickness. As reference thickness values it has been used an already studied structure by the literature on the matter ($35nm/10nm/20nm$).

In the first case fig(2.14) as one increases from $5nm$ to $55nm$ the top MoO_3 layer thickness, a change of the shape is appreciated as well as a general red shift of the transmittance. If one plots the wavelength corresponding to the maximum value of the curve, as one can see in fig(2.12) this yields a linear tendency towards larger values of the wavelength. This is an interesting result to take into account because easy tuning of the maximum on the transmittance spectrum can be used to match transmitted light with silicon absorbance in order to ensure greater carrier generation on the cell.

The averaged transmittance has been calculated using typical solar power distribution at Air mass 1.5 (i.e Air mass coefficient defines optical path length

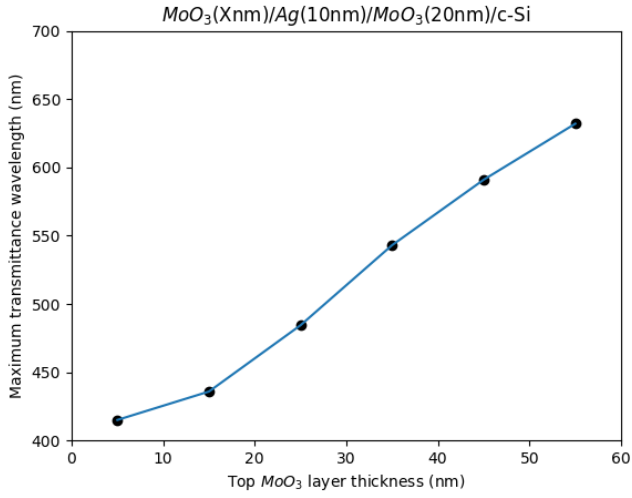


Figure 2.12

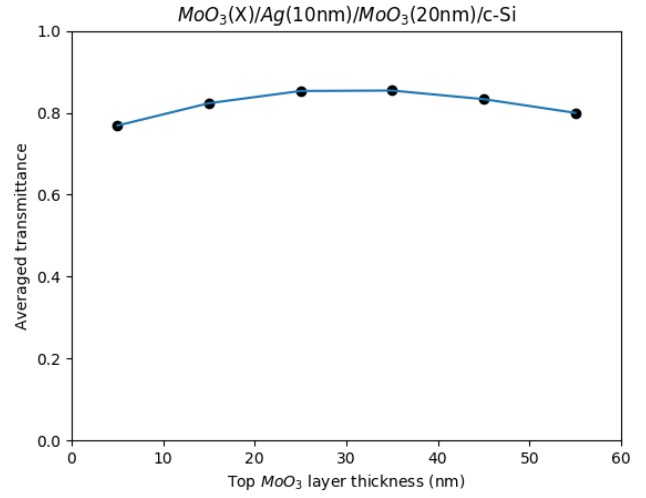


Figure 2.13

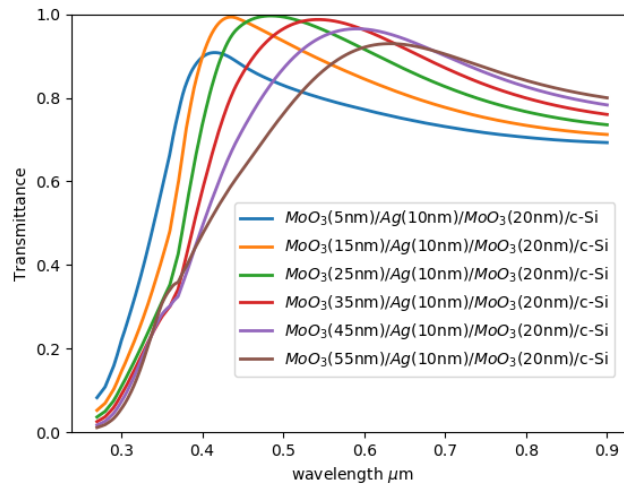


Figure 2.14

through the Earth's atmosphere), by means of:

$$T_{average} = \frac{\int_{270nm}^{900nm} T(\lambda) AM_{1.5}(\lambda) d\lambda}{\int_{270nm}^{900nm} AM_{1.5}(\lambda) d\lambda}$$

As one can see in fig(2.13), average transmittance yields a maximum near the 30nm zone. This result is consistent with averaged transmittance tendency measured in [34]. Even though a mismatch of over 20% on the transmittance is

accounted by different spectrum integration process, ranges and most important perhaps model mismatch.

Comparing measured values of the maximum transmittance wavelength [21] as a function of top dielectric thickness, with the structures that have been simulated, one can see how simulated and measured values follow a biased linear tendency in fig(2.15). This result yields remarkable resemblance if only behaviour with the layer thickness is considered, and gives reliability to the tendency obtained in the simulation. On the other hand results on the simulation differs from the one slope linear fit diminishing credibility on the actual values obtained.

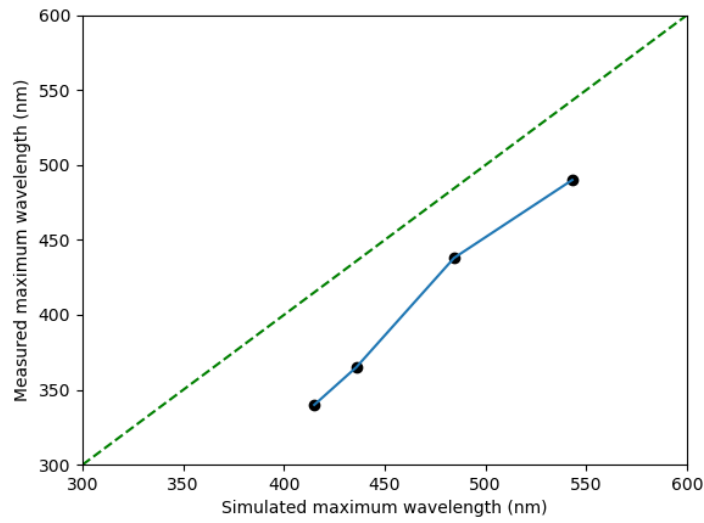


Figure 2.15

When top MoO_3 layer thickness is fixed and bottom layer effect is studied one observes consistent but different tendencies.

As seen in fig(2.18) one can intuitively see faster red shift of the spectrum. If as done for the top layer this red shift is quantified and plotted as seen in fig(2.16), one can see that the structure also follows a linear tendency but the maximum of the curve is displaced to larger values than for the top case. This yields a greater sensitivity of the system to changes in the bottom dielectric layer.

When averaged transmittance in fig(2.17) is compared with measured values in [34], a maximum between $10nm$ to $20nm$ still holds for simulated results, as well as a drop of transmittance as one increases bottom layer thickness. So for the bottom MoO_3 layer besides the divergence on the average transmittance value, as for the top dielectric layer, a similar tendency holds for the simulation results.

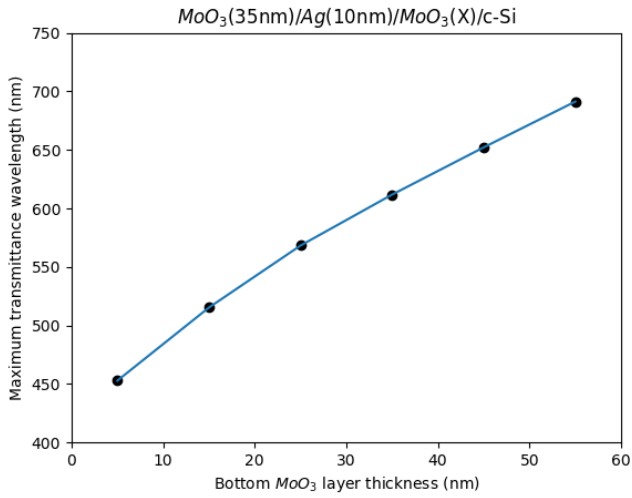


Figure 2.16

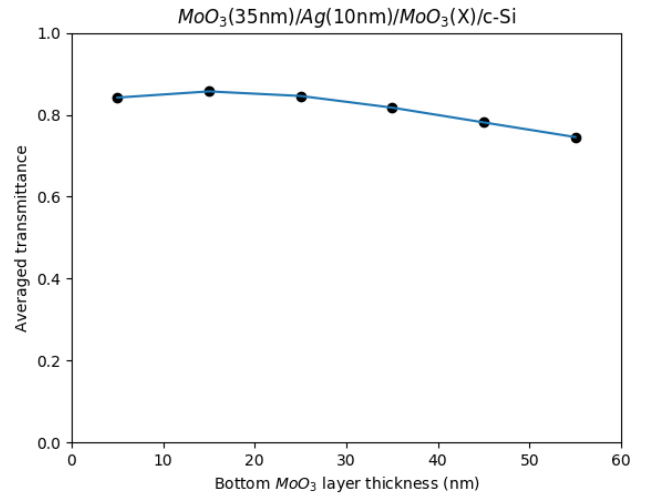


Figure 2.17

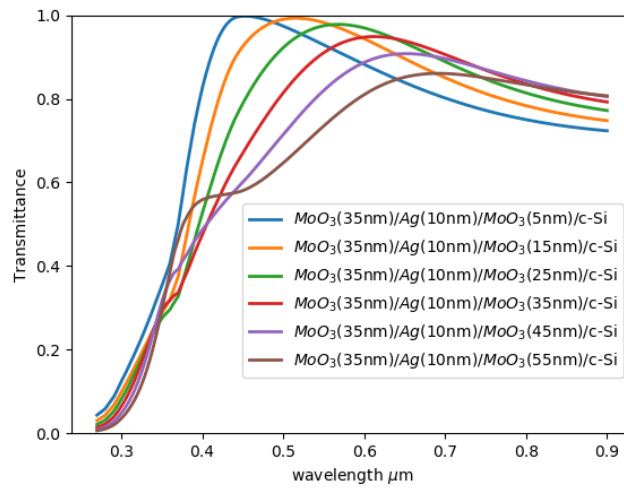


Figure 2.18

If one goes to extreme cases, such as very high thickness of the top and bottom MoO_3 layers, one finds strange results that may be due to computation mismatch with reality or optical interference caused by large thickness of the top/bottom layers.

As the averaged transmittance slowly decreases with a smooth tendency in fig(2.20) and fig(2.23), this rough change seen in fig(2.19) for the top dielectric layer and in fig(2.22) for the bottom one, looks like a natural change of the system, but

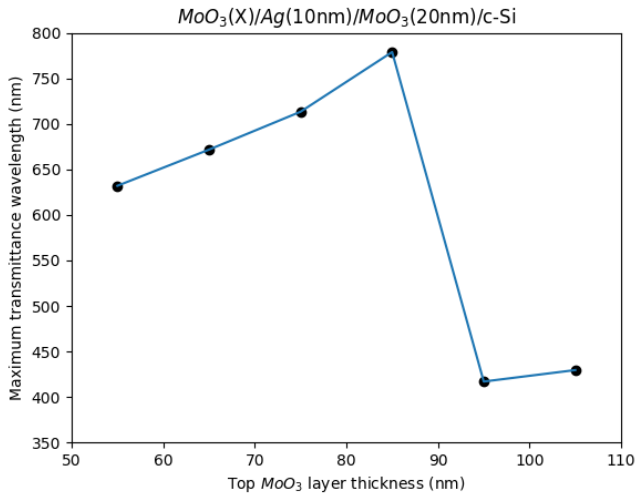


Figure 2.19

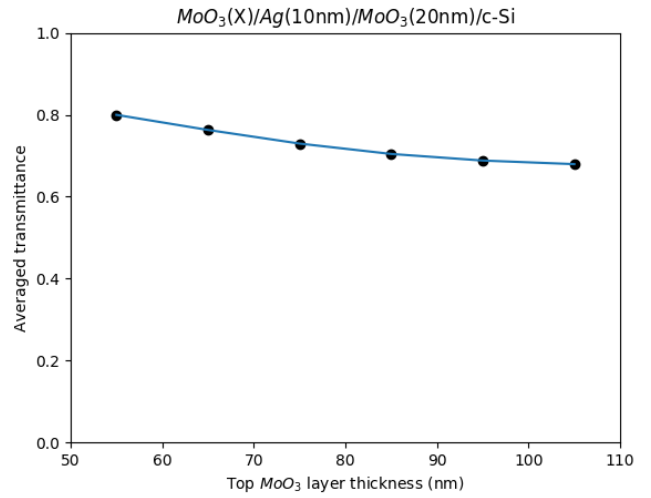


Figure 2.20

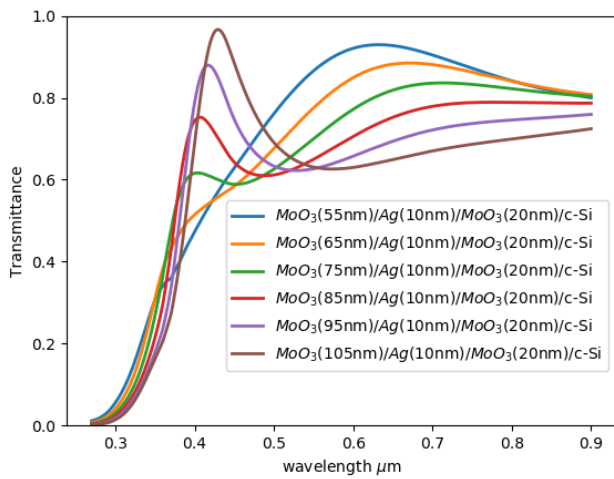


Figure 2.21

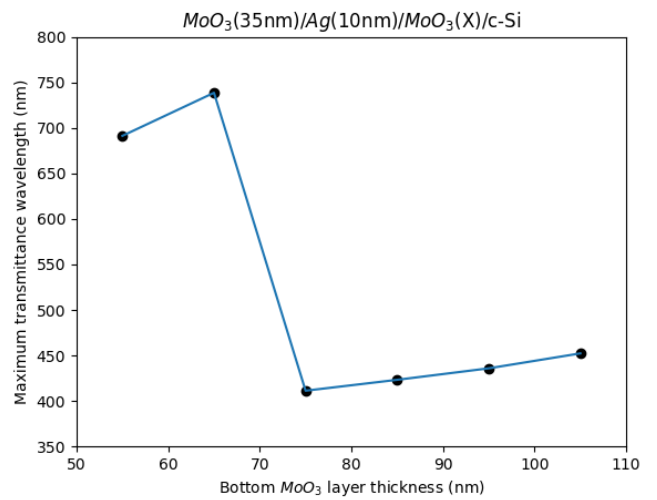


Figure 2.22

no optical information on DMDs with this dielectric thickness have been reported so a definitive conclusion can't be extracted from this results.

Simulations on optical properties have stated that enhanced light transmittance through the device is achieved using a configuration near $35nm/10nm/20nm$ values.

Nevertheless this results kept fixed to the already known "optimal" value one of the dielectric layers, so a $2D$ mapping of the transmitted light seems a more

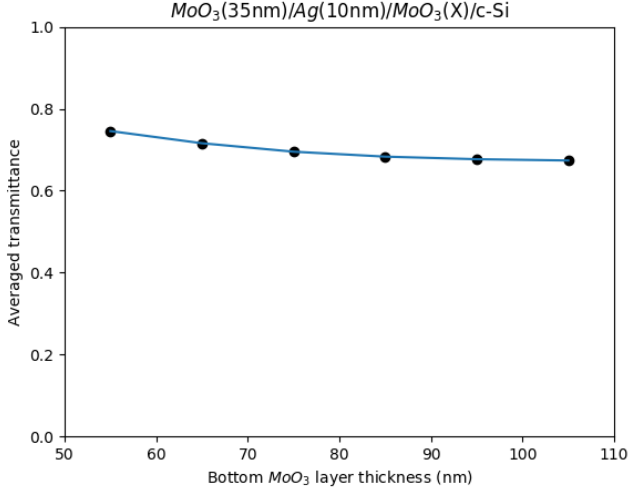


Figure 2.23

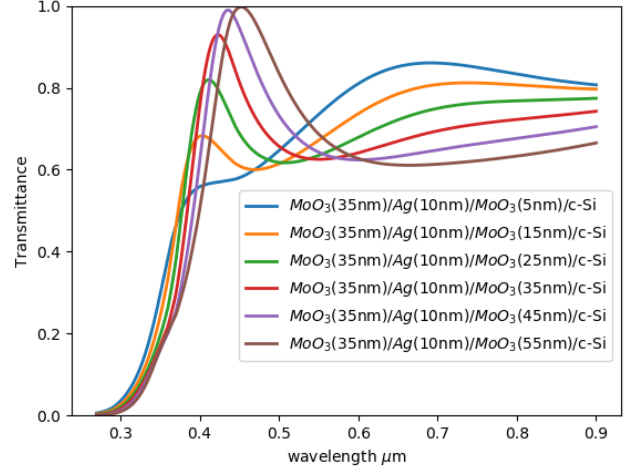


Figure 2.24

efficient way to find optimal dielectric thicknesses as anti reflection coatings on solar cells.

Since one of the goals is to apply this technology to solar cells one can directly transform optical transmittance into photo generated current of the cells by means of the previously introduced Air Mass 1.5. Transmitted power density becomes $T_p(\lambda) = T(\lambda)AM_{1.5}(\lambda) \sim \frac{w}{m^2 \cdot nm}$. By means of unity conversion one can get $\frac{w}{m^2 \cdot nm} \propto \frac{J}{s \cdot m^2 \cdot nm}$, if each photon generates an electron-hole pair with the energy of the absorbed photon (hc/λ) and charge e one gets $\frac{J}{s \cdot m^2 \cdot nm} \cdot \frac{C}{J} \propto \frac{A}{m^2 \cdot nm}$.

Once this transformations have been done a spectral integration through the desired window of the spectrum is done to find the value of the photo generated current, as in silicon not all of the wavelengths are absorbed and much less for thin wafers, an exponential factor depending on the absorption coefficient of silicon and the wafer thickness, assumed to be $d = 300\mu m$, has been added to the overall computation on the form of:

$$J_{ph} = \int_{\lambda_{low}}^{\lambda_{up}} T_p(\lambda)(1 - e^{-\alpha(\lambda)d})d\lambda \sim \left(\frac{mA}{cm^2}\right)$$

For the case under study a setup of the type ($MoO_3/Ag/MoO_3/SiO_2/c - Si$) has been used with inclusion of a native oxide layer of $4nm$ thick, finally the final photo current map obtained from TMM method can be seen in fig(2.25).

For validation purposes one can see how photo current simulation map obtained in [29], and represented in fig(2.26), by means of comercial raytrace software (i.e *Wafer Ray Tracer simulation tool, PVLighthouse Pty.Ltd*) matches perfectly with

obtained windows of maximum photo current generated. Furthermore a second window of increased photocurrent has been found for large thickness of the bottom dielectric layer. Even though photo current generation doesn't match the same scale due to simplicity implied in the model used, as in this model all absorbed photons are transformed into electron/hole pair and collected without any recombination, shadowing of the contacts, or ohmic losses taken into account.

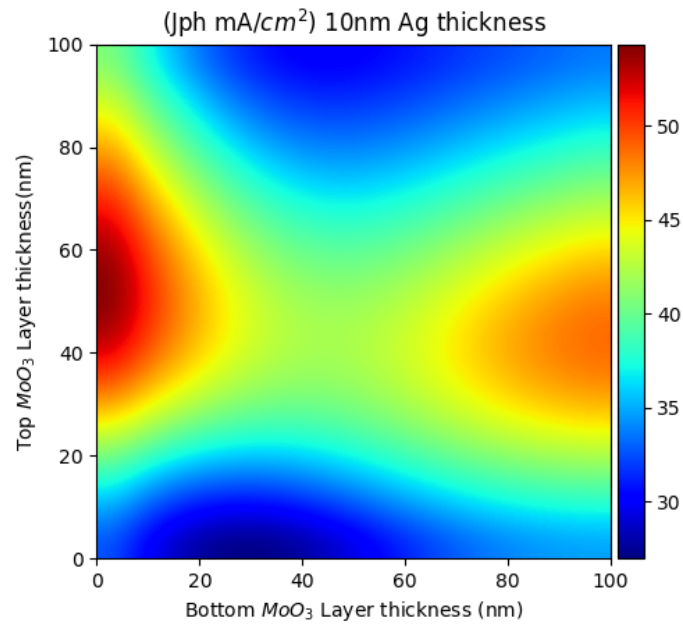


Figure 2.25

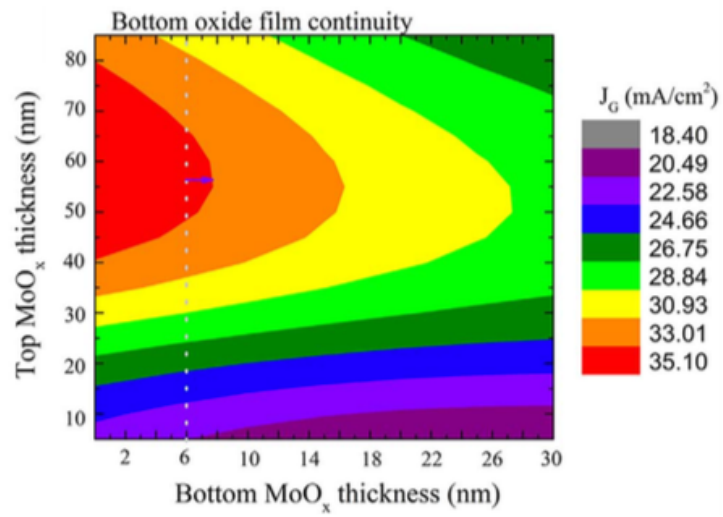


Figure 2.26

Chapter 3

Fabrication and characterization of DMD structures

3.1 Equipment and facilities

MBRAUN Glove Box evaporator

In this work Glove Box evaporator is the most fundamental machine when one is referring to the fabrication of this structures. Located outside the clean room and with a N_2 atmosphere, O_2 concentration inside the glove box is controlled always under 2-3 *ppm*. The glove box mainly works as a clean environment when manipulating, fabricating or keeping samples for further purposes. Inside the Glove Box one has 2 vacuum chambers for organic and inorganic and metallic evaporation. Since basics of thin film growth and evaporation have already been covered in **Section(2.2)** no further explanation on the evaporation process will be done. Vacuum chamber is connected to a mechanical and turbo-molecular vacuum pump. Growing rate of the layers is controlled through the *INFICON SQC – 310TM* thin film deposition controller read of two quartz sensors, and manually controlled with a shutter that shadows the path of the molecules when turned desired.

Procedure for DMD evaporation consist on preparing and cleaning of a substrate sample (e.g glass, silicon wafer ...) and evaporate the different layers on top.

When evaporation is done turbo-molecular pump is turn off by means of N_2 insufflation inside the chamber.

Clean Room environment and equipment

Typically used in scientific research when a low level of environmental pollutants such as dust, aerosol particles, and chemical vapors is required. The clean room consists on an environment with a high control on level of contamination by typical airborne particles, as well as temperature, pressure and humidity, for reproducibility of results when environment sensitive materials or techniques are used.

Special suits have to be wear when one is inside the clean room, as well as an air bath for disposing out of the suits some of the otherwise potential contaminants such as dirt, dust, hair and other biological or inorganic materials.

Inside the clean room one disposes of several machines that have been used for this research:

Perfilometer: The profilometer mainly consists on a thin needle that can measure nanometric dimension steps. It was used when calibrating the readings of deposited MoO_3 and Ag thickness in the Glove Box evaporator. Other checking measures have been done such as thickness measures of the whole DMD multilayer coating, and thickness of the deposited silver contacts on final solar cell.

Sinton photoluminescence detector: This photoluminescence detector was used to study life time of the carriers and implicit open circuit tension of a silicon wafer with deposited DMD on top as well as for sheet resistance measures.

4 point probe: Injecting current from two probes and measuring tension from the other two, one finds in this method a fast way to measure sheet resistance without the need of evaporating contacts and avoiding contact resistance. It was used as main measure when evaluating conductivity of fabricated DMD structures. Maximum resistance read of this machine is over $1000 \Omega/sq$ which for non conducting samples is orders of magnitude below the real resistance measured with transfer length method.

Atomic Layer Deposition: Using known precursors that when mixed react with the material surface, ALD can deposit layers with nanometric scale precision. It was used for alumina and titanium dioxide deposition in the first attempted solar cell.

Plasma enhanced chemical vapour deposition: Commonly used technique in solar cells when amorphous silicon deposition is required. Inside a vacuum chamber precursor gas are introduced and radiofrequency is applied until a plasma is achieved. Plasma gas is then condensated onto the surface. It was used for i/n a-Si:H ETL deposition in second attempted solar cell

RF magnetron sputtering: Argon gas is ionized inside a vacuum chamber by radio frequency excitation and collision of the Ar ions with target sends particles of the desired materials in gas form that condensates onto the substrate surface. Used for ITO deposition in reference fabricated cell with $Al_2O_3+TiO_2$ ETL.

Lithography: A photoresist coating is deposit onto the wafer and UV illu-

mined onto desired active zone, this is to remove photoresist from the active area where dmd will be deposited. It was done as part of the fabrication process of the solar cells.

Measure Room environment and equipment

The measure room consists on a well equipped room for all type of electronic measurements (e.g solar cells, transistors, integrated circuitry). Machines used in this work from this room consist on

Solar simulator lamp: Consists on a lamp with similar spectrum to the emitted by the sun. J-V characteristics of the cell in dark conditions were measured using regular oscilloscope and in light conditions with the light obtained from this lamp.

External quantum efficiency: EQE is defined as the ratio between the collected charge carriers and the incident photons as a function of the incident light wavelength. The EQE is calculated by direct illumination of the solar cell with a laser source and measure of the current intensity produced by the solar cell. Equipment that measures this curve have been used for solar cell characterization.

UB facilities

Under *Joan Bertomeu* supervision, optical measures on fabricated DMDs were done in the *photo-spectrometer* machine of UBs measure room.

SEM and TEM microscopy imaging were done in *Centres Científics i Tecnològics de la Universitat de Barcelona*.

3.2 Fabrication process

Sample cleaning

Before the DMD deposition, a profound cleaning of possible contaminants from the surface of the substrate is done. As part of a systematic procedure a cleaning process is done to each borosilicate glass sample used consisting on :

- 1) Pressured nitrogen shower on the glass sample is done to remove large particles attached to the surface of the glass, procedure is done with metallic tweezers holding the sample.

- 2) Acetone bath is done to remove any possible organic compound.

- 3) Propanol/isopropanol bath is done to the sample as part of cleaning procedure and as a help to remove residual acetone on the glass.

- 4) Unionized water is used as a final sample cleaner to remove any residual trace of potential contaminants.

5) Changing to Teflon tweezers a N_2 gas shower is done again to remove the water from the sample and once most of the water is removed and visually looks drop-free, it is left to dry in a case (cleaned with the same procedure) inside the glove box for later use.

For the case of Silicon wafers used in the study only a Fluorhydric acid cleaning was done to remove native oxide before deposition of the DMD and ETL layers.

Evaporation

Sample is located onto target of the evaporator and attached by means of a small Kapton layer on the corners of the glass/silicon. Once the target is properly placed on its spot and the vacuum chamber has achieved a pressure of at least $8 - 9 \cdot 10^{-6} mbar$, one can start evaporating. Evaporation of the materials is done without breaking the vacuum since the chamber disposes of two crucibles for different materials. Tweezers manipulation of the samples after and before evaporation has to be done carefully thus it may result on scratching of the glass or the DMD. This has proven to be critical to electric properties when measured sheet resistance.

3.3 Fabrication and characterization of $MoO_3/Ag/MoO_3$ structures

3.3.1 $MoO_3/Ag/MoO_3/Glass$ structures

In the first attempt to fabricate and study MAM multilayer coatings, different experiments were thought to approach structure fabrication and parameters optimization. A series of bottom and top evaporation with fixed thickness of the other layers to optimize dielectric layers as done in [34] or a series of depositions studding the effect of different thickness of the metallic layer as done for most of the literature on the topic [29,33,35,36,37,38] were the two main options. Finally it was decided to attempt reproduce the results obtained in [33].

For a first batch of DMDs of $(20nm/X/35nm)$ where X studied was from $2.5nm$ to $10nm$ in $2.5nm$ steps deposited at very low rate. Obtained results can be seen in fig(3.1), as one can see ITO/glass has a stable high transmittance all along the spectrum, while for fabricated DMDs as one increases silver thickness absorption is dramatically affected and layers become rather of a bluish opaque colour.

On fig(3.2), an averaged transmittance is plotted as a function of the silver layer thickness. Besides ITO averaged transmittance is also plotted and corresponds to the purple line with a value of 75.46%. On the averaged values of the transmittance

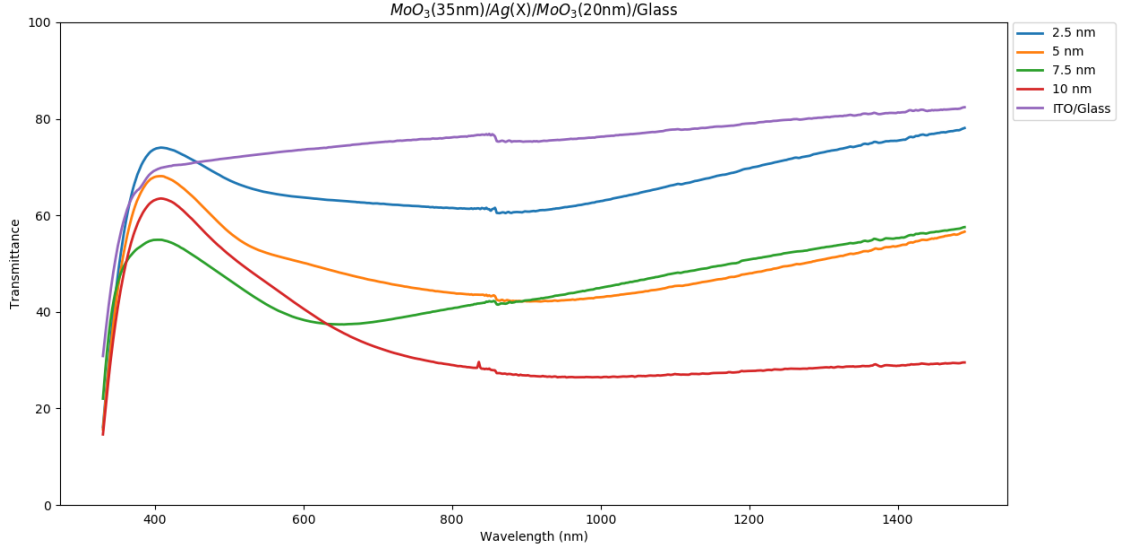


Figure 3.1

of this first batch of DMDs one finds how quickly drops the transmittance when the silver layer is increased.

As opposition to what literature states in [21], an increase on the silver layer should represent an increase on the transmittance of the DMD as the silver layer becomes homogeneous and the surface roughness decreases. This kind of results yielded a problem during evaporation of the samples. Even though at a silver thickness of 7.5nm one can see an increase of the transmittance on the larger wavelengths, on the overall average it still holds a lower optical transmittance. *4-point prove* method was performed on the samples to study its conductivity, and insulator like behaviour of the structure was obtained. As part of double checking methodology, a *Transfer length method* was performed on the samples to find whether a high contact resistance of the *4-point prove* affected the measures or the samples were actually behaving like insulators.

Results yielded a sheet resistance of the order of hundreds of Mega Ohms ($R_{sh} \sim 100M\Omega$).

First hypothesis when this results were obtained was that deposition of the silver layer was not smooth, and thus most probably *Volmer-Webber* type of growing of the silver layer was the major concern that would affect sample optical and electrical properties.

Improved conductivity of the structures was desired. As one can see in [33] deposition rate of the silver layer has proved to be a major factor when thermally

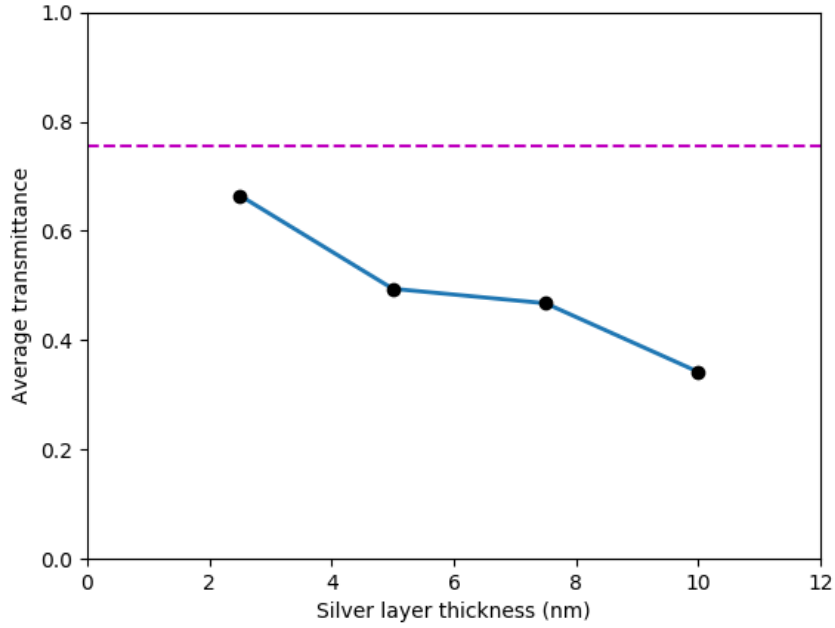


Figure 3.2

evaporated ultrathin silver layers are desired to be smooth. Therefore for the rest of the samples the deposition rate of the silver layer was fixed at $4\text{\AA}/s$, and for Molybdenum trioxide at $1\text{\AA}/s$.

To see if, for this fixed values of the deposition rate, one would still achieve topologically rough and percolated silver layers, $Ag(X)/MoO_3(20nm)/Glass$ samples were fabricated with the same previously studied silver thicknesses. Field Emission Surface Electron Microscopy (FE-SEM) was performed on this samples in order to study the topography of the surface on the deposited metallic layers. 20 nm MoO_3 seed layer was deposited on top of the glass to observe the behaviour of silver in similar working conditions (i.e DMD).

For the $2.5nm$ silver layer it was impossible to achieve a clear image of the topography of the surface, this could indicate that material deposition onto the MoO_3 was very low and resolution of FEM was not enough to distinguish silver aggregations. This would certainly account for low conductivity of the $2.5nm$ silver layer DMD.

For $5nm$ thick silver layer as seen in fig(3.3), one can clearly see opaque regions on the picture that account for the percolation paths. While for $7nm$ thick silver layer seen in fig(3.4), the deposited layer become less granular and one can clearly

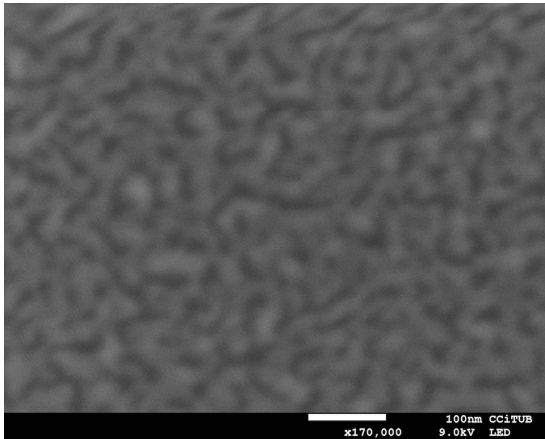


Figure 3.3

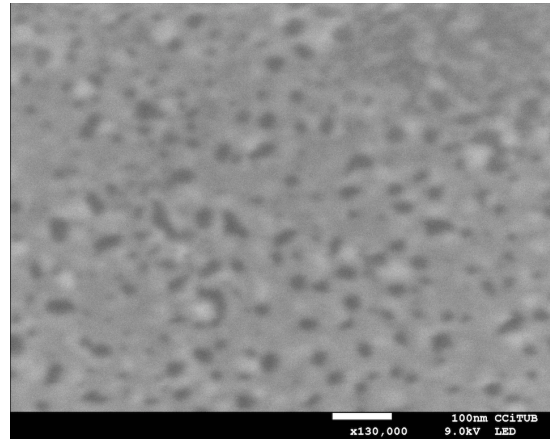


Figure 3.4

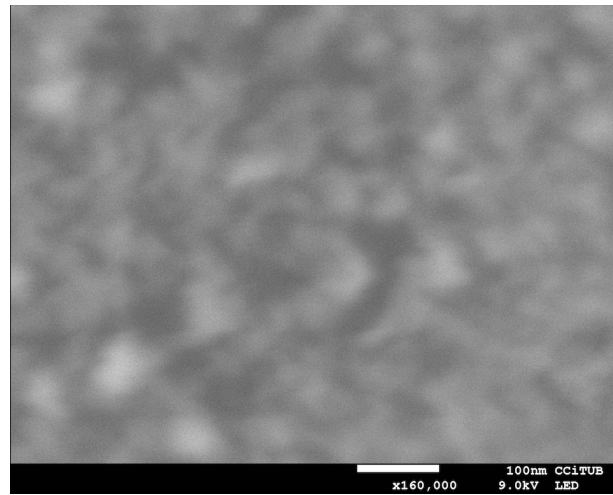


Figure 3.5

see that overall percolation of the structure is reduced.

Finally with the $10nm$ silver layer seen in fig(3.5), one can see how the surface looks topologically rough even though homogeneous. Therefore, one might think that with these fixed deposition conditions one should achieve $35nm/10nm/20nm$ -MAM DMDs with proper electrical properties.

As one would expect for the next batch of fabricated DMDs, conductivity of the $10nm$ thick silver layer had improved by many orders of magnitude.

	$R_{sh}^{MAM} (\Omega/sq)$	$R_{sh}^{MA} (\Omega/sq)$
$t_{Ag} = 2.5nm$	1125	900
$t_{Ag} = 5nm$	1125	10
$t_{Ag} = 7.5nm$	1125	13
$t_{Ag} = 10nm$	16	0.6

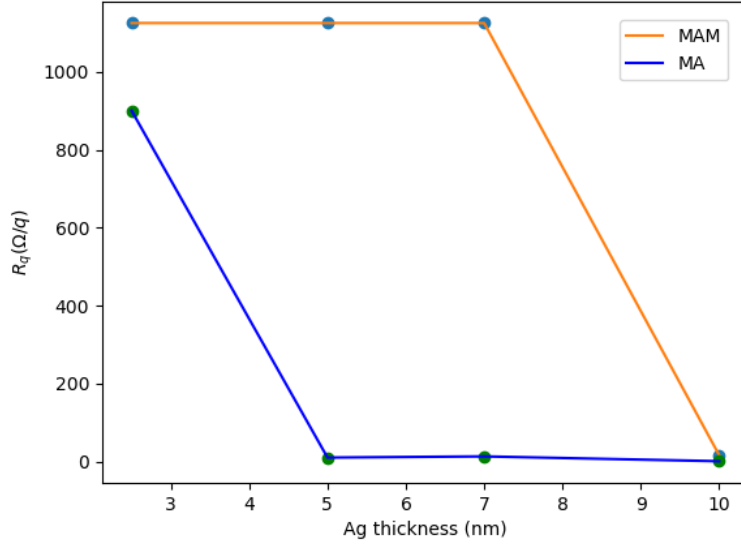


Figure 3.6

Interesting to notice how in fig(3.6), one can see an increase of the silver thickness conduction threshold due to the top deposited dielectric layer. Which would indicate that despite what was introduced in **Section(2.3)**, conduction on this multilayer structure could be more complicated than just parallel distribution of the resistances.

Finally one can see in fig(3.8) how conducting DMD sample 20/10/35 (nm) also has achieved better optical properties than non conducting DMD with the same layer thickness. This can be attributed to the frequency change of the surface plasmons of the percolated structure as the new structure has an homogeneous metallic layer.

Interesting fact about this new batch of optimized samples is transition from a high transparent state to a bluish less transparent colour as can be seen in fig(3.7). One can see how just evaporated sample is more transparent, than the sample deposited one week before. New averaged transmittance of the sample spikes up to 54% which is still to be improved to more near ITO values. But

on applications where transmittance is not as critical as in solar cells one could already study behaviour of devices with MAM transparent conducting layers.

Unstable super-transparent state of this improved DMDs and degradation process it follows is still to be determined. Since samples were kept inside the N_2 environment of the glove box either a reaction between the deposited compounds or a post deposited aggregation of the pseudo-homogeneous silver layer could explain the time scale degradation of optical properties. Nevertheless electrical properties measured after degradation process remained at same values, which could indicate also that the degradation occurs on the molybdenum oxide layer. In conclusion a completely closed hypothesis of the mechanics involved in this degradation process has not been obtained.

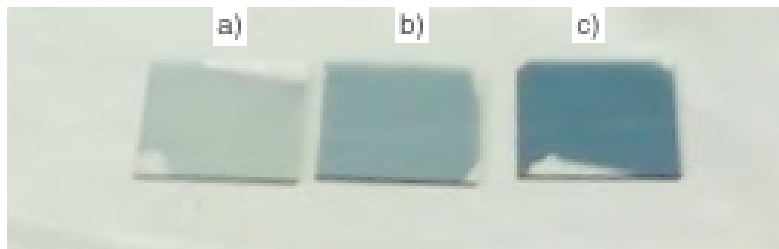


Figure 3.7: **a)** Recently evaporated 20/10/35 (nm) sample **b)** One week old 20/10/35 (nm) sample **c)** Non conducting 20/10/35 (nm) sample

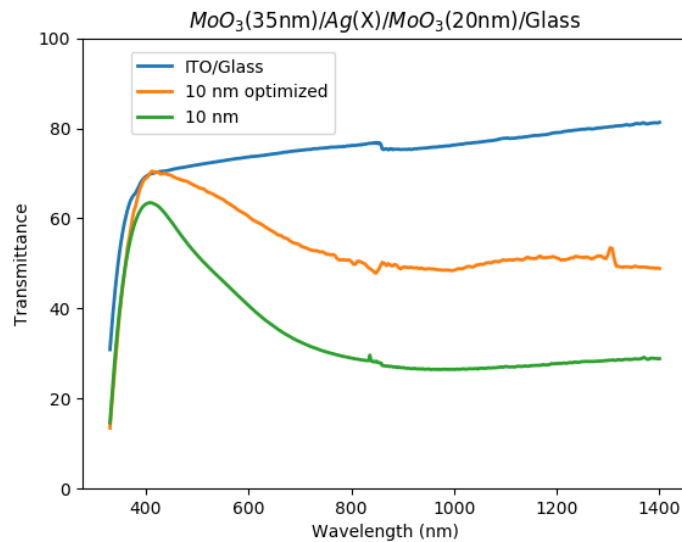


Figure 3.8

3.3.2 $MoO_3/Ag/MoO_3/c-Si$ structures

Behavior of DMD layers have been studied when *c*-Si wafer is used as a substrate instead of glass.

When first FE-SEM images were obtained, it was thought that glass surface roughness (i.e. $\pm 3\text{nm}$) could affect the behaviour of the already visualized metallic layer, as the characteristic roughness of the glass is more or less of the same order of magnitude than the layers that are aimed to deposit. This could yield a different behaviour of this multilayer when substrate is changed to silicon, that has an extraordinary surface flatness. To study the resultant morphology of this trilayer coating when deposited on top of *c*-Si, a 20/10/35-MAM sample was subjected to Focused Ion Beam (FIB) to cut a cross section of the multilayer and via HRTEM imaging observe the different morphologies of the layers.

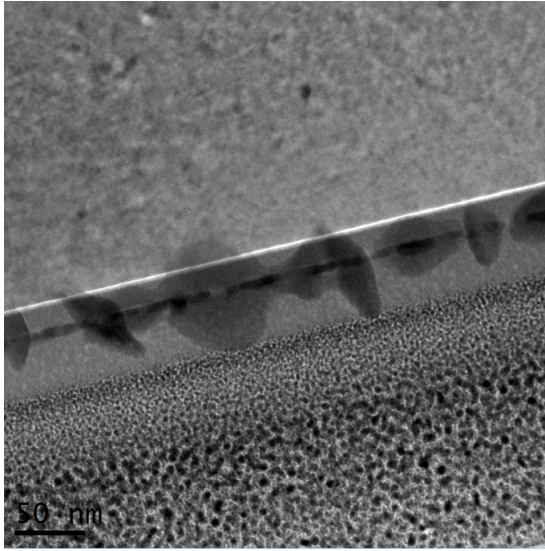


Figure 3.9

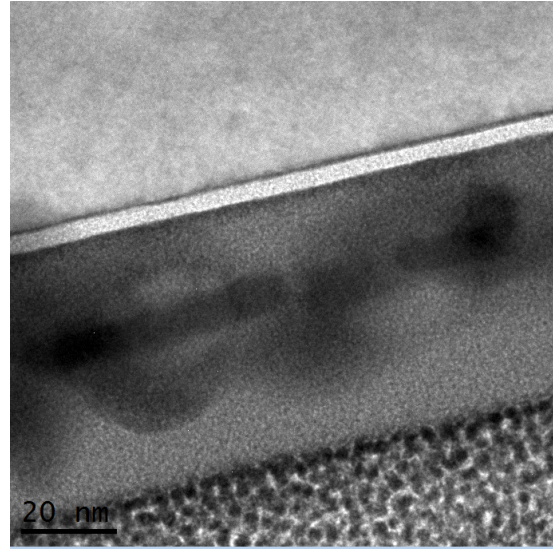


Figure 3.10

As can be seen in different transversal cuts of the multilayer a great diffusion of the silver is observed which could be a potential problem for optical transmittance and account for the optical degradation observed and explained in the previous section. Even though it is thought that the greater ranges of observed diffusion (i.e. anti intuitive diffusion of the silver inside the silicon, and silver diffusion reaching the top surface of the molybdenum oxide layer), are consequence of the high energetic FIB procedure. This procedure could trigger an increased mobility on the *Ag* atoms outside of the sample transversal cut. Besides this procedure triggered diffusion, agglomeration of the silver is still appreciated while surface roughness is rather eliminated.

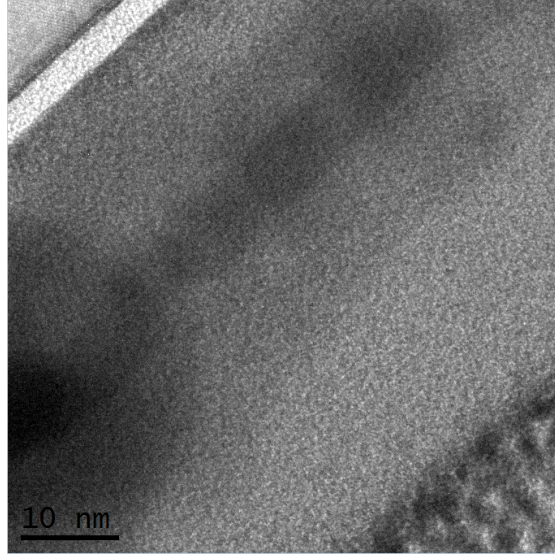


Figure 3.11

Unexplained obtained results of optical degradation of DMDs properties was a major concern on the long time behaviour of fabricated solar cells. Using recent investigation of the group [39], Al_2O_3 passivation layer and TiO_2 ETL was deposited at the bottom of a n-type silicon wafer, while on the top, 15/9/35 (nm) and 15/11/35 (nm) MAM DMDs were deposited.

Using sinton photoluminescence detector, two weeks evolution of the life time of the minority carriers and implicit open circuit tension has been measured as one can see in table below.

Degradation of the bottom ETL layer is out of the question since reference ITO+ MoO_3 wafer with the same Alumina and Titanium dioxide layer as ETL did not show any degradation of the life time or implicit open circuit tension.

With this results one can think that the observed drop of the carriers life time and implicit open circuit voltage measured by the photoluminescence detector, could be related to the unknown process that decreased optical transmittance on the glass samples.

Further study of the time dependence and the cause of this degradation must be done in order to ensure environmentally stable DMDs.

	$\tau^{(15/9/35)}$ (μs)	$\tau^{(15/11/35)}$ (μs)	$V_{oc}^{(15/9/35)}$ (mV)	$V_{oc}^{(15/11/35)}$ (mV)
10-20 min after evaporation	168	167	607	616
2 weeks after evaporation	105	120	595	606

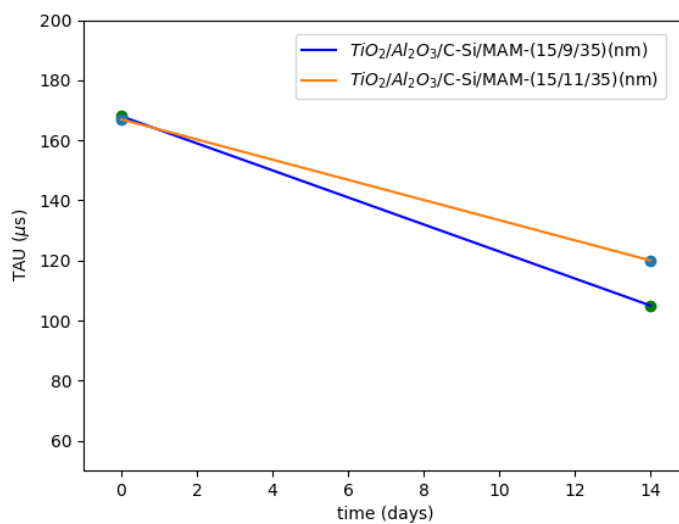


Figure 3.12

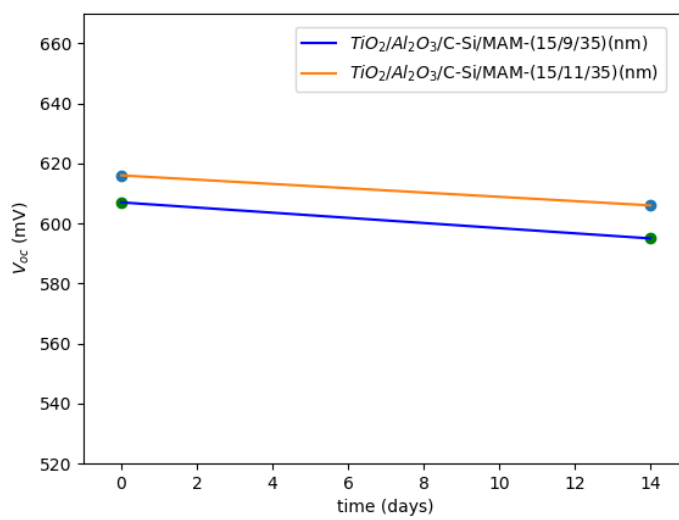


Figure 3.13

Chapter 4

Fabrication and characterization of top electrode DMD c-Si solar cells

4.1 Design and fabrication of DMD based solar cell

Two type of solar cells were tested in this work, using for both cases a top deposition of MAM DMDs tested solar cells differed on the deposition of Al_2O_3/TiO_2 or classical *a*-Si:H (n) as the the bottom ETL.

Fabrication process decided for both cells have been illustrated from fig(4.1) to fig(4.5) for the alumina passivation layer and titanium dioxide ETL and from fig(4.6) to fig(4.9) for the amorphous silicon ETL.

On a quick summary for the first types of cells, a thin layer of Al_2O_3/TiO_2 is deposited by ALD on the top and bottom surfaces of the silicon wafer. Afterwards a metallic deposition of Magnesium and Aluminum as posterior contact is done. At this stage lithography is done to define active area and protect posterior contact from HF done to remove top of Al_2O_3/TiO_2 layer. Finally DMD is deposited on top of the wafer photoresist is removed from the bottom contact and the silver contacts are evaporated .

With the amorphous silicon cell, used procedure was rather similar. Amorphous (i/n) layer was grown by PECVD on the bottom surface of the wafer as the ETL of the cell. Lithography is done to define active area and protect bottom ETL layer of posterior HF attack. Once HF is done DMD is deposited on the top of the cell. The photo resist is then removed from the bottom layer and as a final step silver and aluminum contacts are evaporated.

As one can see DMD was deposited on all of the top wafer area, and wasn't

removed afterwards of the non active area. This was due to believe that abrupt change of the height on the edge of the photoresistor with the active area was enough to isolate the cells. Furthermore step of removing the photoresistor with acetone was thought to affect the DMD multilayer.

Besides the DMD based solar cells a classical TMO solar cell (i.e ITO+ MoO_3) was fabricated with the alumina and titanium dioxide bottom ETL as a reference solar cell.

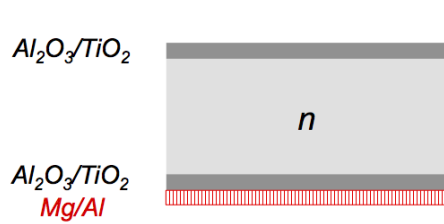


Figure 4.1

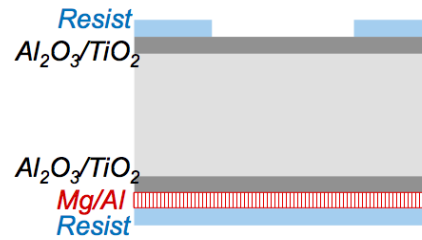


Figure 4.2

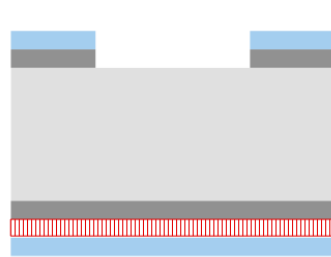


Figure 4.3

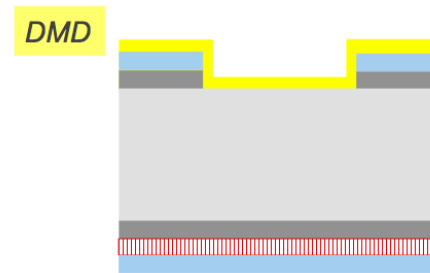


Figure 4.4

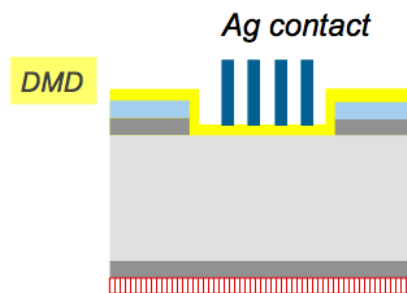


Figure 4.5

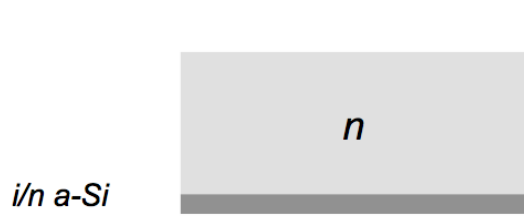


Figure 4.6

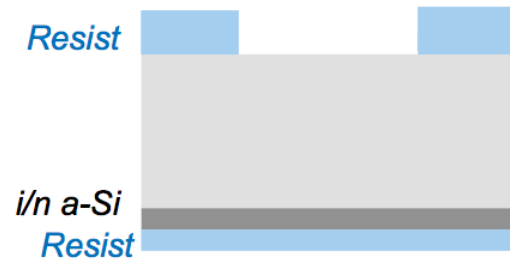


Figure 4.7

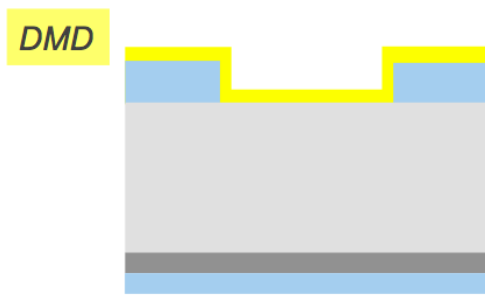


Figure 4.8

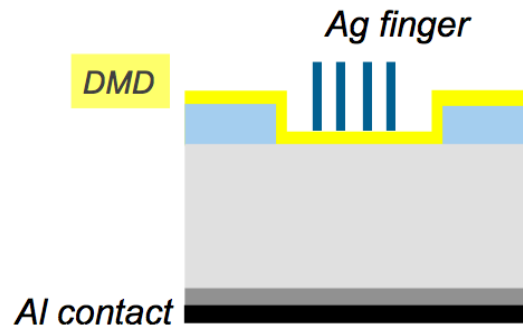


Figure 4.9

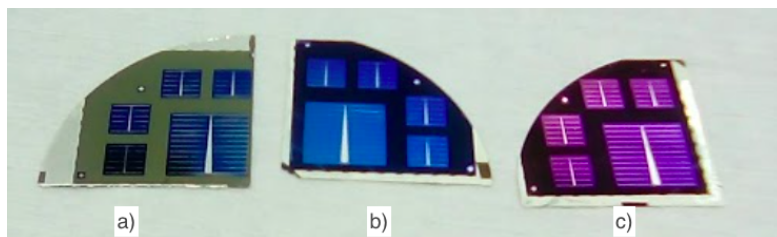


Figure 4.10: **a)**Reference ITO+ MoO_3 solar cell **b)** 35/11/15 nm DMD solar cell **c)** 35/9/15 nm solar cell

4.2 Characterization of DMD based solar cell

Analysis of the obtained data from the characterization can give us an idea on whether this technology is a good or bad fit to the replace TMO+ITO top selective contact and conductive antireflection layer in solar cells.

From the external quantum efficiency measurements performed on the TiO_2 ETL solar cells in fig(4.11) one can see how collection of the generated carriers of the indium free cells is below the ITO reference. As one should expect the 9 nm silver layer DMD has an increased EQE on shorter wavelengths than the 11 nm layer. This can be attributed to less absorption of the metallic layer. Still EQE values achieved for DMD based solar cells are far below the MoO_3 +ITO reference.

On the other hand maximum EQE values achieved for the ITO reference are over 70%. This contrasts with Luis G. Gerling *et al* measurements in [41] where EQE for this type of cells reached near 90% values. This fact and lift off problems during lithography procedure could indicate that fabrication of this cells was compromised, and with further improvement of the fabrication method one could achieve larger EQE for the DMDs cells.

From figures 4.12 and 4.13 one can see how the cells perform in dark conditions. For the (i/n) a-Si:H ETL one can see how the cell with a intrinsic a-Si buffer below the DMD as a passivant layer performs poorly, with a noisy signal. As for the (i/n) a-Si:H ETL without the buffer one can see that a greater current-tension relation of the diode than with the buffer. For the Al_2O_3 - TiO_2 ETL the difference on the silver layer thickness can be seen on higher tension values.

Regarding the performance under light conditions as one can clearly see the cell with amorphous silicon ETL and the intrinsic buffer is short-circuited, yielding a very poor performance. As for the cell without the intrinsic buffer one can see how a great passivation of the rear side due to the use of a-Si has an impact on the FF and therefore a PCE of 5.99% is achieved. For the titanium dioxide ETL solar cells one can see a PCE of about 4.90% of both 35/9/15 and 35/11/15 (nm) DMD. A slightly greater photocurrent in the 9 nm thick silver layer DMD may be associated to less absorption of the metallic layer in the DMD structure. Less Fill factor of the 9 nm silver layer DMD cell may be also associated to higher series Resistance due to the less amount of silver deposited.

Thus, as can be seen in table below, it can be clearly stated that there is a compromise between PCE related parameters (i.e V_{oc} , J_{sh} , FF) and DMD characteristic parameters (i.e optical transmittance (T%), electrical conductivity (R_{sh}), passivation of MoO_3 bottom layer). This is of course besides the bottom ETL related parameters. Furthermore, optimization of the PCE related parameters can't be done on an individual level since multiple relations between this parameters affect the overall performance of the cell, and probably best way to approach

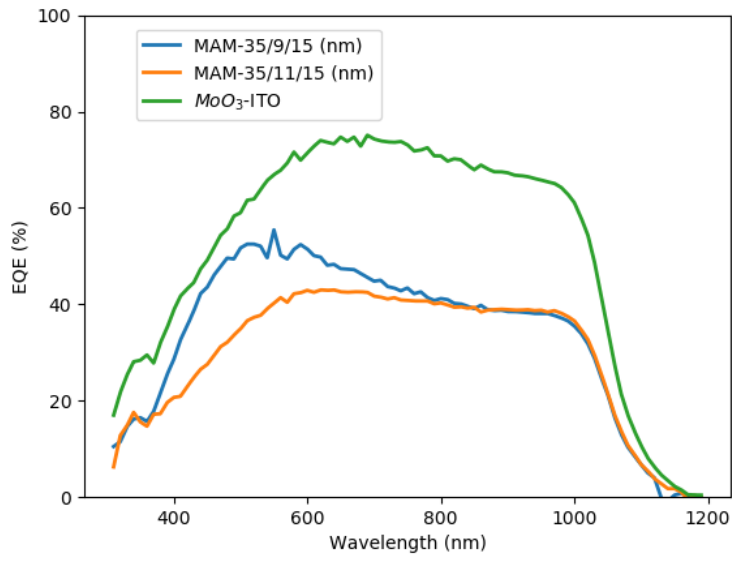


Figure 4.11

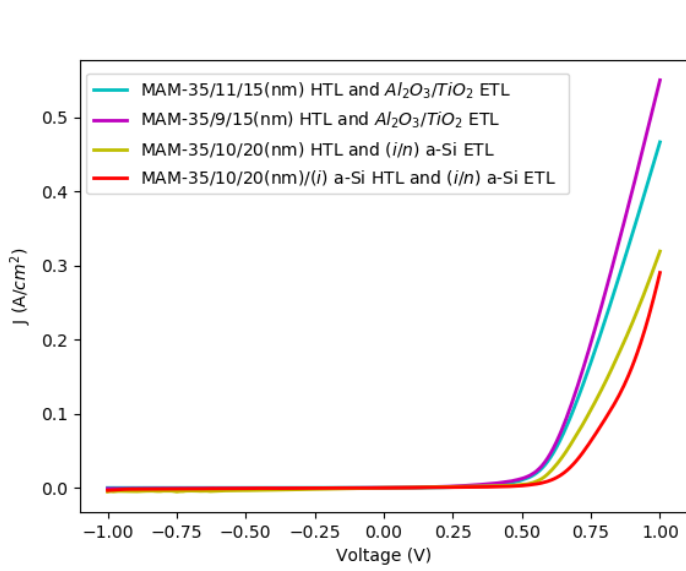


Figure 4.12

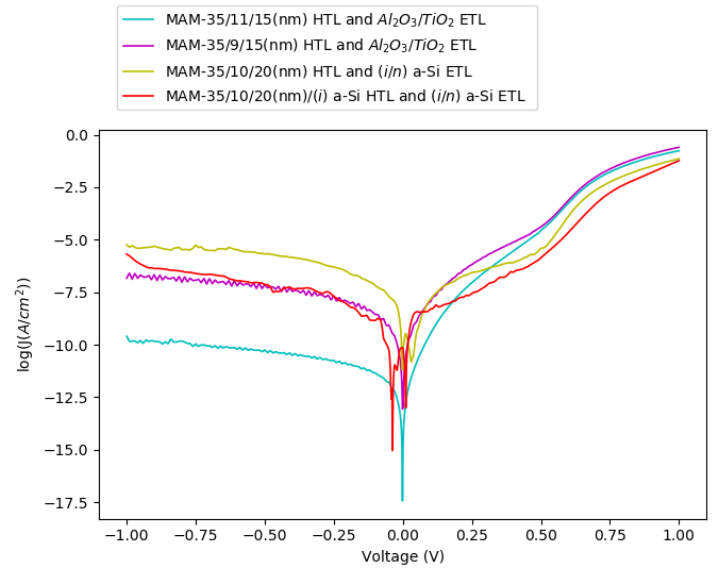


Figure 4.13

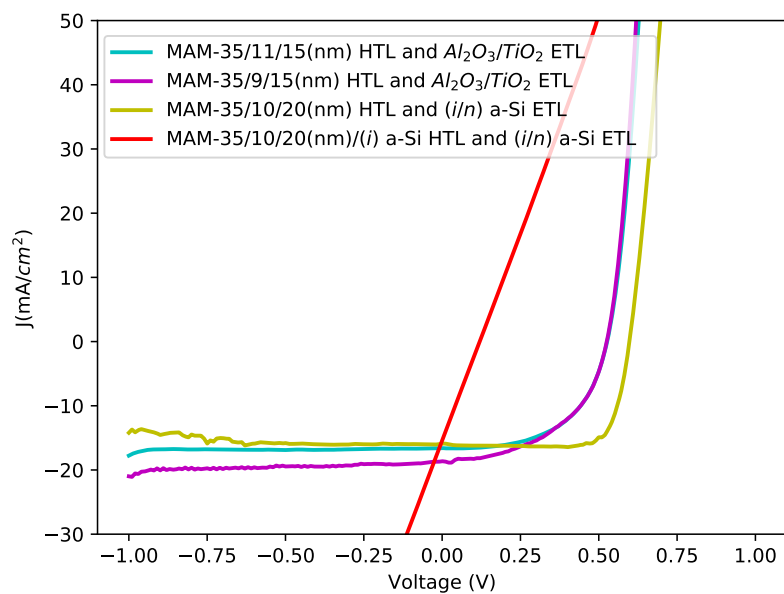


Figure 4.14

	V_{oc} (V)	FF (%)	J_{sc} (mA/cm^2)	PCE (%)
15/9/35 (nm)(TiO_2 ETL)	0.525	50.42	18.73	4.89
15/11/35 (nm)(TiO_2 ETL)	0.526	56.78	16.61	4.9
20/10/35 (nm)($a-Si$ ETL)	0.585	65.03	15.97	5.99
20/10/35 (nm)($a-Si$ ETL/ (i) buffer)	0.118	26	15.49	0.5

Chapter 5

Conclusion and future work

Great effort of this research has been dedicated on starting and improving a fabrication methodology of dielectric metal dielectric based conductive transparent layers, using the UPC *Electronic Engeneering department* facilities and machinery. Besides a broad amount of simulations regarding optical properties of this structures have been done using *Transfer Matrix Method* in order to optimize top and bottom dielectric thicknesses, and understand the behaviour of this kind of multilayer coatings.

Simulation results of the transmittance when top and bottom dielectric thickness is changed on a 35/10/20 (nm) yielded a linear relation with real structures results measured on [21]. With this direct relation between reality and simulations one can use TMM results as a guide to choose optimal dielectric thicknesses. On the other hand transmittance simulation results obtained diverged from the actual measured values mainly as a consequence of the model simplicity. Future work in this aspect could lead to more complex simulations regarding FDTD method, complex geometries and use of effective index of thin layers measured by ellipsometry.

On the technological aspect of this work, literature results on behaviour of the DMD optical and electrical properties structures with the metallic mid layer thickness have been successfully reproduced. Furthermore a never reported super-transparent state of the DMD when the conductivity threshold thickness is deposited that degrades to a less transparent state has been observed. Degradation mechanism has not been completely understood but it's been seen that degradation does not affect electrical conductivity and affects optical transmittance minority carriers life time and implicit open circuit tension, this last two when deposited on a n-type silicon wafer with Alumina and Titanium dioxide as passivation layer and ETL on the bottom.

Based on the topography study of the metallic mid layer, silver deposited on the conductivity threshold thickness would either diffuse inside the dielectric layer, or

aggregate back to a possible percolated thermodynamically speaking more stable state. Future work could regard the study of larger thicknesses of silver to see if this degradation effect is avoided. Besides this the use of Au or Al seed layers to see if this super-transparent state is stabilized is still an open possibility.

Conduction of Molybdenum oxide and silver (MA) interface as a function of the silver thickness has been studied as well as the typical MAM configuration. It's been seen that ultrathin silver layers (i.e 5 and 7.5 nm) show conductive behaviour, while when 35 nm MoO_3 is deposited on the top, the threshold is displaced to higher silver thickness (i.e 10 nm). This results yield a more complex model on the conductivity of this structures than parallel association of resistances.

Finally two types of ETL bottom contact solar cells have been tested with top DMD selective contact. A maximum PCE of 5.99% and 4.9% for the (i/n) a-Si:H and $Al_2O_3+TiO_2$ respectively show that improvement is yet to be done to the fabrication method and DMD depositions. Since most part of this work effort was to optimize the 20/10/35 (nm) structure, variations close to this structure were deposited when the cells were fabricated. Still future work will consist on deposit optimization of top and bottom thickness close to the maximum photogenerated current found in the simulation.

Nevertheless implicit V_{oc} of 6.16 mV measured on the silicon wafer with bottom TiO_2 ETL, and maximum values achieved of $FF = 65\%$ for (i/n) a-Si:H ETL solar cell and $J_{sc} = 18.73mA/cm^2$ for the TiO_2 ETL solar cell, yields that with further optimization of the layers thicknesses and deposition, as well as the fabrication procedure of the solar cell, an increase of the overall efficiency of this new type of indium free solar cells is still to be achieved.

Conference presentations

Research done in this project has been used for the group in several symposiums as poster presentations, either by direct presentation of the results obtained or as collaboration with *Raül Perea* TFG:

- J. Puigdollers, L.G. Gerling, G. Masmitja, *E. Ros*, R. Perea, P. Ortega, C. Voz, R. Alcubilla, "Carrier selective contacts based on V_2O_5 -Ag- V_2O_5 structures", European Materials Research Society Spring Meeting (E-MRS), Strasbourg, France (2017).
- J. Puigdollers, L.G. Gerling, G. Masmitja, *E. Ros*, R. Perea, P. Ortega, C. Voz, R. Alcubilla, "Carrier selective contacts based on dielectric/metal/dielectric structures", 9th International Conference on Materials for Advanced Technologies (MRS), Singapore (2017).

- C. Voz, R. Perea, L.G. Gerling, *E. Ros*, J.M. Asensi, J. Puigdollers, J. Andreu, J. Bertomeu, “Transition-metal-oxide hole-selective contacts by RF magnetron sputtering for heterojunction silicon solar cells”, 9th International Conference on Materials for Advanced Technologies (MRS), Singapore (2017).

Bibliography

- [1] Characterization and optimization of ITO thin films for application in hetero-junction silicon solar cells: Shui-Yang Liena*, Chin-Cheng Leeb, Dong-Sing Wuuc, Ray-Hua Horngd, Min-Yen Yehb
- [2] Skotheim, Terje A. Reynold, John “Handbook of Conducting Polymers” CRC Press, 1998 ISBN 0-8247-0050-3
- [3] Metal-nanostructures – a modern and powerful platform to create transparent electrodes for thin-film photovoltaics: Kirill Zilberberg and Thomas Riedl*, Cite this: DOI: 10.1039/c6ta05286j
- [4] Characterization of Transition Metal Oxide/Silicon Heterojunctions for Solar Cell Applications. Luis G. Gerling *, Somnath Mahato †, Cristobal Voz, Ramon Alcubilla and Joaquim Puigdollers
- [5] Transition-Metal-Oxide hole-selective contacts by RF magnetron sputtering for heterojunction silicon solar cells, .Voz, Cristobal; Perea, Raül; Gerling, Luis G.; Ros, Eloi; Asensi, Jose M.; Andreu, Jordi; Puigdollers, Joaquim; Bertomeu, Joan
- [6] Edwards, P. P.; Porch, A.; Jones, M. O.; Morgan, D. V.; Perks, R. M. (2004). ”Basic materials physics of transparent conducting oxides”. Dalton Transactions (19): 2995–3002. doi:10.1039/b408864f. PMID 15452622.
- [7] Minami, Tadatsugu (2005). ”Transparent conducting oxide semiconductors for transparent electrodes”. Semiconductor Science and Technology. 20 (4): S35. Bibcode:2005SeScT..20S..35M. doi:10.1088/0268-1242/20/4/004.
- [8] Review article: Polymer-matrix Nanocomposites, Processing, Manufacturing, and Application: An Overview Farzana Hussain, Mehdi Hojjati, Masami Okamoto and Russell E. Gorga Journal of Composite Materials 2006; 40; 1511 DOI: 10.1177/0021998306067321

- [9] Toward Real Applications of Conductive Polymers Hans H. Kuhn, Andrew D. Child and William C. Kimbrell Milliken Research Corporation P.O. Box 1927, M-405 Spartanburg, South Carolina 29304
- [10] Flexible transparent conductors based on metal nanowire networks Chuan Fei Guo and Zhifeng Ren* Department of Physics and TcSUH, University of Houston, TX 77204, USA.
- [11] P. Würfel, Physics of Solar Cells, from Principles to New Concepts. WILEY-VCH, 2005.
- [12] R. Hall, "Electron-Hole Recombination in Germanium," Phys. Rev., vol. 87, no. 2, pp. 387–387, Jul. 1952.
- [13] W. Shockley and W. Read, "Statistics of the Recombinations of Holes and Electrons," Phys. Rev., vol. 87, no. 5, pp. 835–842, Sep. 1952.
- [14] Quantum Transport: Atom to Transistor, Supriyo Datta, Cambridge University Press
- [15] U. Wu rfel, A. Cuevas, and P. Wu rfel, "Charge carrier separation in solar cells", IEEE Journal of Photovoltaics 5, 461–469 (2015).
- [16] S. Datta. Electronic Transport in Mesoscopic Systems, Cambridge 1997.
- [17] P. Wu rfel, Physics of solar cells: from principles to new concepts (John Wiley Sons, 2008).
- [18] Jaeger, Richard C. (2002). "Film Deposition". Introduction to Microelectronic Fabrication (2nd ed.). Upper Saddle River: Prentice Hall. ISBN 0-201-44494-1.
- [19] L. Vj, N. P. Kobayashi, M. S. Islam, W. Wu, P. Chaturvedi, N. X. Fang, S. Y. Wang, R. S. Williams, "Ultrasoother Silver thin films deposited with a Germanium nucleation layer," Nano. Lett. 9, 178-182 (2009).
- [20] C. Guille n and J. Herrero, Thin Solid Films 92, 938 (2008)
- [21] Toward indium-free optoelectronic devices: Dielectric/metal/dielectric alternative transparent conductive electrode in organic photovoltaic cells L. Cattin*,1, J. C. Berne'de2, and M. Morsli3 1 Universite de Nantes, Institut des Mate riaux Jean Rouxe DOI 10.1002/pssa.201228089
- [22] C. Guille n and J. Herrero, Thin Solid Films 520, 1 (2011).

- [23] S. Y. Ryu, J. H. Noh, B. H. Hwang, C. S. Kim, S. J. Jo, J. T. Kim, H. S. Hwang, H. K. Baik, H. S. Jeong, C. H. Lee, S. Y. Song, S. H. Choi and S. Y. Park, *Appl. Phys. Lett.*, 2008, 92, 023306.
- [24] Y. C. Han, M. S. Lim, J. H. Park and K. C. Choi, *Org. Electron.*, 2013, 14, 3437–3443.
- [25] S. Lim, D. Han, H. Kim, S. Lee and S. Yoo, *Sol. Energy Mater. Sol. Cells*, 2012, 101, 170–175.
- [26] Dielectric/metal/dielectric structures using copper as metal and MoO₃ as dielectric for use as transparent electrode. I. Pérez López a, L. Cattin a, D.-T. Nguyen a, M. Morsli b, J.C. Bernède c, Université de Nantes, Institut des Matériaux Jean Rouxel. *Thin Solid Films* 520 (2012) 6419–6423
- [27] Improvement of Transparent Metal Top Electrodes for Organic Solar Cells by Introducing a High Surface Energy Seed Layer. Sylvio Schubert,* Jan Meiss, Lars Müller-Meskamp, and Karl Leo DOI: 10.1002/aenm.201200903
- [28] Ultrasmooth and Thermally Stable Silver-Based Thin Films with Subnanometer Roughness by Aluminum Doping Deen Gu, Cheng Zhang, Yi-Kuei Wu, and L. Jay Guo*, Department of Electrical Engineering and Computer Science, University of Michigan, 10.1021/nm503577c
- [29] Multilayer MoO_x/Ag/MoO_x emitters in dopant-free silicon solar cells. Weiliang Wua et al. 12/09/2016 . <http://dx.doi.org/10.1016/j.matlet.2016.11.059>
- [30] O. S. Heavens, *Optical Properties of Thin Films* Dover, New York, 1965 , p. 69.
- [31] M. Born and E. Wolf, *Principles of Optics* MacMillan, New York, 1964 , p. 254.
- [32] <https://www.refractiveindex.info>
- [33] Effect of the Ag deposition rate on the properties of conductive transparent MoO₃/Ag/MoO₃ multilayers. L.Cattin *et al.* *Solar Energy Materials Solar Cells* 117 (2013) 103–109
- [34] Effect of the thickness of the MoO₃ layers on optical properties of MoO₃/Ag/MoO₃ multilayer structures. D.-T. Nguyen, J. C. Bernède *et al.* *Journal of Applied Physics* 112, 063505 (2012); doi: 10.1063/1.4751334

- [35] Indium-free multilayer semi-transparent electrodes for polymer solar cells. Alexander T. Barrows, Rob Masters *et al.* <https://doi.org/10.1016/j.solmat.2015.10.010>
- [36] Top illuminated organic photodetectors with dielectric/metal/dielectric transparent anode. Hyunsoo Kim, Kyu-Tae Lee *et al.* <https://doi.org/10.1016/j.orgel.2015.02.012>
- [37] Improved conductivity and mechanism of carrier transport in zinc oxide with embedded silver layer. H. Han, N. D. Theodore, and T. L. Alford. Citation: J. Appl. Phys. 103, 013708 (2008); doi: 10.1063/1.2829788
- [38] Effect of silver evolution on conductivity and transmittance of ZnO/Ag thin films. Citation: Journal of Applied Physics 109, 104318 (2011); doi: 10.1063/1.3592975
- [39] V2Ox-based hole-selective contacts for c-Si interdigitated back-contacted solar cells. Gerard Masmitjà, Luís G. Gerling, Pablo Ortega, Joaquim Puigdollers, Isidro Martín, Cristóbal Voz and Ramón Alcubilla. DOI: 10.1039/c7ta01959a
- [40] Fabrication and surface plasmon coupling studies on the dielectric/Ag structure for transparent conducting electrode. Rina Pandey, Basavaraj Angadi, *et al.* Interface Control Research Center, Korea Institute of Science and Technology
- [41] Transition metal oxides as hole-selective contacts in silicon heterojunctions solar cells. Luis G. Gerling, Somnath Mahato, *et al.* Electronic Engineering Department, Universitat Politècnica de Catalunya. 42 E cient silicon solar cells with dopant-free asymmetric heterocontacts James Bullock *et al.* DOI: 10.1038/NENERGY.2015.31
- [42] EFFECTS OF DIFFERENT WETTING LAYERS ON THE GROWTH OF SMOOTH ULTRA-THIN SILVER THIN FILMS, Thesis Submitted to The School of Engineering of the UNIVERSITY OF DAYTON By Chuan Ni Dayton, Ohio August, 2014.